IEEE Access
Multidisciplinary ⋮ Rapid Review ⋮ Open Access Journal

Received 23 July 2024, accepted 1 September 2024, date of publication 4 September 2024, date of current version 13 September 2024.

Digital Object Identifier 10.1109/ACCESS.2024.3454220

RESEARCH ARTICLE

Fractional-Order Modeling and Steady-State Analysis of Single-Phase Quasi-Z-Source Pulse Width Modulation Rectifier

XIAOQUAN ZHU[1], **(Senior Member, IEEE), ZIWEN CHEN**[1], **AND BO ZHANG**[2], **(Fellow, IEEE)**
[1]College of Automation Engineering, Nanjing University of Aeronautics and Astronautics, Nanjing 211106, China
[2]School of Electrical Power, South China University of Technology, Guangzhou 510641, China

Corresponding author: Xiaoquan Zhu (ijruexq@nuaa.edu.cn)

This work was supported in part by the National Natural Science Foundation of China, under Grant 62201256; and in part by the Fundamental Research Funds for Central Universities under Grant 56XAA21057.

ABSTRACT This paper focuses on the fractional-order modeling and analysis of single-phase quasi-Z-source rectifier (qZSR), aims to extend the single-phase qZSR from integer-order domain to fractional-order domain. Additionally, it has been demonstrated explicitly the mechanism by which fractional-order inductors (FOIs) and fractional-order capacitors (FOCs) affect the operating features of fractional-order quasi-Z-source rectifier (FO-qZSR). The fractional-order circuit model is built based on oustaloup's approximation method, the operational principle and control strategy of FO-qZSR, the expression of input current, inductor current, capacitor voltage and output voltage are also derived and analyzed in detail. Then, the above theoretical analysis is verified by simulation results by using the fotf toolbox in Matlab/Simulink, and the FO-qZSR presents more flexible and diverse operating features than integer-order qZSR. Finally, the hardware prototype is established with the help of the RT-LAB platform and the experimental results are consistent with the theoretical analysis and simulation results.

INDEX TERMS Fractional calculus, fractional-order inductor, fractional-order capacitor, fractional-order PID controller, quasi-Z-source rectifier.

I. INTRODUCTION

With the advent of fractional calculus concept, the way we explore the world has been extended from integer-order to fractional-order field, the mathematics of non-integer order derivative and integration are defined in [1] and [2]. And the researchers found that fractional-order models offer a better explanation of system dynamics than integer-order models [3], [4]. With the in-depth research and development of fractional calculus theory for the past few years, fractional calculus has been widely concerned and used in electrical engineering field [5].

Inductors and capacitors are critical components in power electronic converters. It is generally realized that they are integer-order components in conventional circuit modeling and researches. With the development of the fractional calculus and its corresponding applications, it is gradually realized that the characteristics of inductors and capacitors are fractional-order, the real inductors and capacitors are fractional-order components in nature [6], [7], [8], [9], [10], [11]. Jonscher indicates the ideal integer-order capacitors are not existed in nature and the dielectric material used to build capacitors are fractional-order [12], [13]. Jesus demonstrates that different FOCs can be realized by choosing different fractal structures, such as the curves of Koch, Hilbert and Peano [14]. Westerlund indicates that the inductor components in our practical applications have fractional-order characteristics [15]. Machado proposes that the skin effect can help to realize FOI design with different orders [16]. In order to describe the characteristics of the real inductors and capacitors, the appropriate fractional-order models should be established. Researchers can realize approximate

The associate editor coordinating the review of this manuscript and approving it for publication was Ahmed Aboushady.

forms of FOIs and FOCs by rational approximation, such as Carlson method, Matsuda method and Oustaloup's approximation method [17].

Fractional calculus theory provides a novel and efficient method of modeling, control and analysis. And the studies in [18], [19], and [20] show that the operating characteristics of power electronic converters are more realistic and have higher accuracy with fractional-order modeling and analysis. Due to the simple topology and operating characteristics, the majority of current research are mainly focused on fractional-order modeling and analysis of traditional PWM DC-DC converters, for instance, Buck [21], [22], Boost [23], [24] and Buck-Boost converters [25], [26], in both continuous conduction mode (CCM) and discontinuous conduction mode (DCM). While, the research on fractional-order modeling and analysis of inverters and rectifiers are just getting started. For example, the fractional-order model of single-phase PWM rectifier was built, but the influences of inductor order and capacitor order were not analyzed in detail in [27]. The influences of inductor and capacitor orders on the operating characteristics of single-phase PWM voltage-source rectifier were analyzed in [28], but the fractional-order circuit model of the rectifier was not established.

The rectifiers studied above are all conventional voltage source rectifiers, which require that the dc output voltage must be higher than ac input voltage and their rectifier bridges are not allowed to be shoot through [29], [30]. For the conventional current source rectifier, its output voltage must be lower than input voltage and it is forbidden to shoot-through the bridge arm. Therefore, these limitations will limit their application scenarios. Accompanied by the appearance of quasi-Z-source network [31], the single-phase and three-phase quasi-Z-source rectifiers (qZSRs) are proposed. The qZSR can operate in shoot through state, has lower capacitor voltage stress and its dc output voltage is adjustable [32], [33]. Based on the above advantages, researchers started to explore the quasi-Z-source rectifier in many applications [34], [35]. But these quasi-Z-source rectifiers were proposed and analyzed only in the integer-order domain. Fractional-order qZSR was modeled and analyzed in [36], but the detailed operating characteristic analysis and hardware experimental validation are absent.

In addition, with the appliance of fractional calculus theory in the field of control science, fractional-order controllers have gained more attention. In [37], the concept of fractional-order $PI^{\lambda}D^{\mu}$ controller, whose differential and integral orders are both fractional-order was proposed. Four representative fractional-order controllers involving $PI^{\lambda}D^{\mu}$ controller and others were introduced in [38]. Moreover, a method for stabilizing fractional-order system with a fractional-order $PI^{\lambda}D^{\mu}$ controller was presented in [39].

Based on characteristics of FOI and FOC, the fractional-order modeling and analysis of the single-phase qZSR is systematically presented in this paper. The operation principle analysis, modulation and control strategy, impact mechanisms of the orders of FOC and FOI on the operating characteristics are analyzed. The effectiveness of the established fractional-order circuit model and theoretical analysis are confirmed by Matlab/Simulink simulations and experimental results based on the RT-LAB platform.

II. OPERATING PRINCIPLE ANALYSIS OF SINGLE-PHASE FRACTIONAL-ORDER qZSR

Fig. 1(a) shows the circuit symbols of fractional-order inductor and fractional-order capacitor, respectively. The basic symbol for the fractional-order component is a triangle. And α represents the order of FOI and β represents the order of FOC. Fig. 1(b) shows the topology configuration of single-phase FO-qZSR, an ac power grid and a H-bridge are connected to the quasi-Z-source network. The grid side inductor, output capacitor, inductors and capacitors in the

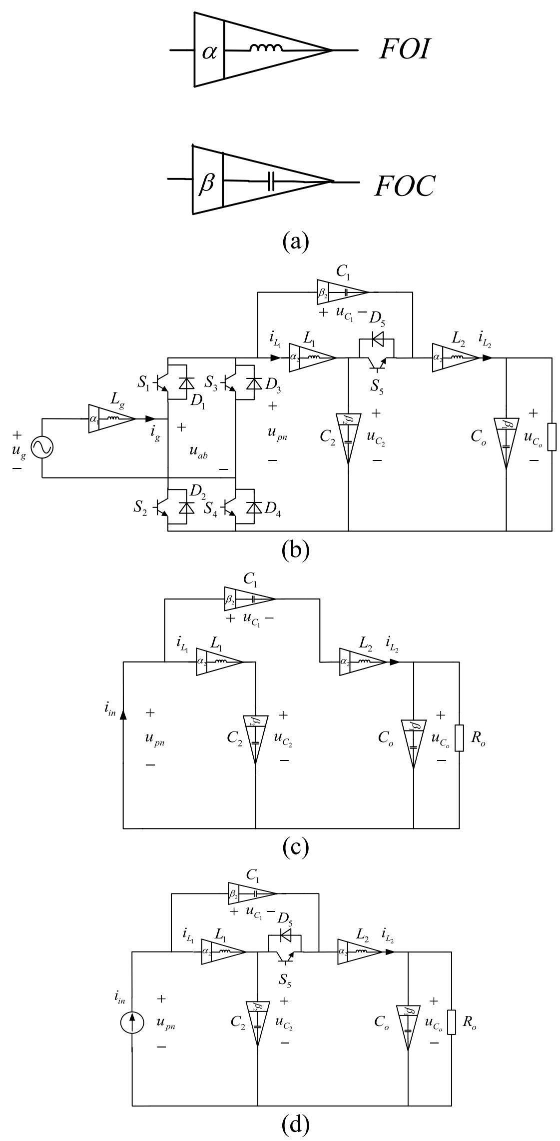

FIGURE 1. (a) The circuit symbols of fractional-order components. (b) The topology configuration of the single-phase FO-qZSR. (c) Equivalent circuit diagram of the FO-qZSR during shoot through state. (d) Equivalent circuit diagram of the single-phase FO-qZSR during non-shoot through state.

quasi-Z-source network are fractional-order components. The order of L_g is α_1 and the order of C_o is β_1. The orders of L_1 and L_2 are α_2, while the orders of C_1 and C_2 are β_2. All of the orders ranges from 0 to 2. In addition, u_g is the grid voltage, i_g is the grid current, S_1-S_5 are power switches, D_1-D_5 are diodes, R_o is the load resistance.

The voltage and current relationship of FOIs and the FOCs can be represented as

$$L\frac{d^\alpha i_L}{dt^\alpha} = u_L, 0 < \alpha < 2 \quad C\frac{d^\beta u_C}{dt^\beta} = i_C, 0 < \alpha < 2 \quad (1)$$

The most significant difference between single-phase quasi-Z-source rectifier and the traditional single-phase voltage source PWM rectifier is that the former allows both power switches of a bridge arm to be turned-on at the same time, which is called the shoot through state. Besides, unlike the quasi-Z-source inverter, the quasi-Z-source rectifier has a power switch rather than a diode in the quasi-Z-source network, which controls the quasi-Z-source rectifier enter into the shoot through state. Hence, there are two operating modes in one switching period. Fig. 1(c) and (d) show the equivalent circuit diagram of each operation mode. Fig. 1(c) shows that when the rectifier is operating in shoot through state, both power switches are turned on at the same time and S_5 is turned off, thus the H-bridge is short-circuit. During this state, the capacitors are charged by inductors, and the inductor currents are decreased. From Fig. 1(c), the following equations can be derived:

$$u_{L_1} = -u_{C_2}, u_{L_2} = -u_{C_1} - u_{C_o}, u_{pn} = 0 \quad (2)$$

where u_{pn} is the dc-link voltage.

During non-shoot through state, as shown in Fig. 1(d), an equivalent current source can represent the H-bridge and S_5 is turned on. In this state, inductors are charged by capacitors, the inductor currents are increased. The following equations can be written by analyzing the operating mode in Fig. 1(d):

$$u_{L_1} = u_{C_1}, u_{L_2} = u_{C_2} - u_{C_o}, u_{pn} = u_{L_1} + u_{C_2} \quad (3)$$

Based on the principle of inductor voltage-second equilibrium, the following equations can be obtained:

$$D(-u_{C_2}) + (1-D)u_{C_1} = 0 \quad (4)$$
$$D(-u_{C_1} - u_{C_o}) + (1-D)(u_{C_2} - u_{C_o}) = 0 \quad (5)$$

where D is the shoot through duty cycle. Based on the above formulas, u_{pn} and u_{C1} and u_{Co} can be expressed by u_{C2}:

$$u_{pn} = \frac{1}{1-D}u_{C_2} \quad u_{C_1} = \frac{D}{1-D}u_{C_2} \quad u_{C_o} = \frac{1-2D}{1-D}u_{C_2} \quad (6)$$

III. CONTROL STRATEGY OF SINGLE-PHASE FRACTIONAL-ORDER qZSR

A. CONTROL STRATEGY

The control block diagram of the single-phase FO-qZSR can be divided into two parts as shown in Fig. 2(a). For the grid side, we use a dual closed-loop controller to control the single-phase FO-qZSR, which is consisted of an grid side current inner-loop of power factor correction and a voltage outer-loop. By applying the dual closed-loop control strategy, we can not only realize unity power factor but also stabilize the capacitor voltage V_{C2} to track the given value. For the dc side, an open-loop voltage control strategy is utilized to control the output voltage. By setting the value of D, the output voltage of single-phase FO-qZSR can be controlled based on the formula (6).

Fig. 2(b) shows the vector diagrams of two possible operation modes on AC side of the rectifier. U_g is the grid voltage, I_g is the grid current, U_{ab} is the AC input voltage of rectifier bridge, U_{Lg} is the voltage of inductor, and U_{Rg} is the internal resistance voltage of grid and inductor. It can be seen that the amplitude and phase of I_g can be controlled by controlling the amplitude and phase of U_{ab}. The basic principle of double closed-loop control is to control the AC input voltage of the rectifier bridge by controlling the modulating waveform, and thus the AC input current can be controlled.

The block diagram of the double closed-loop control is shown in Fig. 2(c). $G_v(s)$ and $G_i(s)$ are the transfer functions for voltage loop and current loop control, respectively. $G_{pwm}(s)$ is the equivalent transfer function of the PWM modulation, and it can be viewed as an inertial link with a very small time constant as

$$G_{pwm}(s) = \frac{k_{pwm}}{1 + sT_s} \quad (7)$$

where $k_{pwm} = u_{pn}/u_{ab}$ is the equivalent gain of the pulse width modulation, and T_s is the switching period.

$G_L(s)$ is the equivalent transfer function of the rectifier AC side.

$$G_L(s) = \frac{1}{sL_g + r} \quad (8)$$

where r is the internal resistance of the grid and inductor.

Besides, $G_{C2}(s)$ is the transfer function from AC input current i_g to capacitor current i_{C2}, and $G_{C2}(s)$ is the transfer function from capacitor current i_{C2} to the capacitor voltage u_{C2}. This article focuses on the selection of parameters for current inner loop control.

To simplify the analysis, the disturbances of AC side voltage are not considered. The control block diagram of the simplified current loop is shown as Fig. 2(d). Based on Fig. 2(d), the transfer function of the current inner loop before FO-PI$^\lambda$ compensation can be obtained as

$$G_{i_g}(s) = \frac{k_{pwm}}{(sT_s + 1)(sL_g + r)} \quad (9)$$

Different from the conventional proportional-integral (PI) current control loop, a fractional-order proportional-integral (FO-PI$^\lambda$) controller is adopted in this paper. The typical mathematical form of FO-PI$^\lambda$ controller is

$$G_i(s) = K_p + \frac{K_i}{s^\lambda} \quad (10)$$

where λ is the integrator order and can be any number between 0 and 2. Since FO-PI$^{\lambda}$ controller has additional adjustable parameters than traditional integer-order PI controller, it provides more flexible adjustability and can achieve a better control effect.

B. TUNING OF FO-PI CONTROLLER

For fractional-order controllers, traditional parameter tuning methods are more complicated, and intelligent optimization algorithms are usually used for parameter tuning, such as pattern search algorithm (PSA), genetic algorithm (GA) and particle swarm optimization (PSO). The PSO algorithm is used in this article to design and optimize the parameters of the fractional-order controller. The flow chart of PSO algorithm is shown in Fig. 2(e).

In the optimization process, by changing the values of the control parameters, the control effect becomes better and the performance index of the system becomes better. The selection of performance index has a significant impact on the quality and speed of optimization algorithms. Integral of absolute (IAE), integral of time-absolute error (ITAE), integral of the square error (ISE) and integral of time-square error (ITSE) are the commonly used methods. In this article, ITAE is utilized, and its definition can be expressed as

$$J = \int_{0}^{\infty} t\,|e(t)|dt \tag{11}$$

where t is the time and $e(t)$ is the error. The sum of the differences between the respective reference and actual values of AC side input current and DC side output voltage is selected as the error in this paper. The effect of large initial errors on performance indexes can be effectively minimized by choosing ITAE as performance index.

In this paper, the PSO algorithm for optimal controller design under ITAE index is used and the process of selecting the control parameters includes the following steps. First, the PSO algorithm assigns each of the possible parameters to K_{p}, K_{i} and λ. Then, these parameters can be brought into the equivalent model of the circuit, and the obtained ITAE index are returned to the algorithm as the fitness. Loop in this manner until the algorithm is exited when the maximum number of iterations is reached, and the optimal solution for the control parameters can be obtained.

Based on the above analysis, the flow chart of the control parameter optimization is shown in Fig. 2(f). By means of the PSO algorithm with ITAE as the index, the problem of solving control parameters is transformed into a problem of finding the best fit for the PSO algorithm based on the ITAE index. Bringing (9) into the PSO algorithm for parameter tuning based on ITAE, the parameters of FO-PI$^{\lambda}$ controller can be obtained finally.

IV. THE MODULATION SCHEME OF SINGLE-PHASE FRACTIONAL-ORDER qZSR

According to the aforementioned operational principle analysis, the single-phase FO-qZSR has shoot-through state and possesses output voltage buck-boost capability. And the process of reducing capacitor voltage stress can be controlled by the shoot-through duty cycle D. Hence, different from the conventional VSR, the single-phase FO-qZSR has three modulation vectors: active vectors, conventional zero vectors, and shoot-through zero vectors, as tabulated in Table. 1.

TABLE 1. The switching states of single-phase FO-qZSR.

Vector	S_1	S_2	S_3	S_4	S_5
Active	0	1	1	0	1
Active	1	0	0	1	1
Conventional zero	0	1	0	1	1
Conventional zero	1	0	1	0	1
Shoot-through zero	0	1	1	1	0
Shoot-through zero	1	0	1	1	0
Shoot-through zero	1	1	0	1	0
Shoot-through zero	1	1	1	0	0
Shoot-through zero	1	1	1	1	0

In order to realize the switching states in Table. 1, the adopted modulation strategy is shown in Fig. 2(g), which has been made some changes based on the multiple frequency sinusoidal pulse width modulation. As shown in Fig. 2(g), $u_a^{*'}$ is obtained by increasing H based on u_a^* ($u_a^{*'} = u_a^* + H$), and $u_b^{*'}$ is obtained by decreasing H based on u_b^* ($u_b^{*'} = u_b^*$ -H). The drive signals of S_1-S_4 are controlled by these four signals, respectively. Thus, the shoot through states can be realized. Furthermore, it can be seen from Fig. 2(g) that the shoot through time is divided into four parts and each of it is inserted separately into the switching process during one switching period, in which the active vector and conventional zero vector are switched from one to the other. The capacitor voltage V_{C2} will not be changed because the shoot through states are inserted into the conventional zero states. In addition, the switching frequency of S_5 is four times that of the $S_1{\sim}S_4$. When S_1, S_2 or S_3, S_4 are turned on, S_5 will be turned off simultaneously. From Fig. 2(g), one can find there is a mathematical relationship between H and D:

$$\frac{H}{2h} = \frac{DT_s/4}{T_s/2} \Rightarrow H = Dh \tag{12}$$

where h is the peak value of the triangle carrier wave, and T_s is the switching period of the single-phase fractional-order quasi-Z-source rectifier.

V. THE OPERATING CHARACTERISTICS OF SINGLE-PHASE FO-qZSR

In order to simplify the analysis of the single-phase FO-qZSR operating characteristics, the elements of FOIs and FOCs in the circuit are divided into two parts, as shown in Fig. 1(b). One contains the grid side FOI and the dc output FOC, the other contains the FOIs and FOCs of the quasi-Z-source

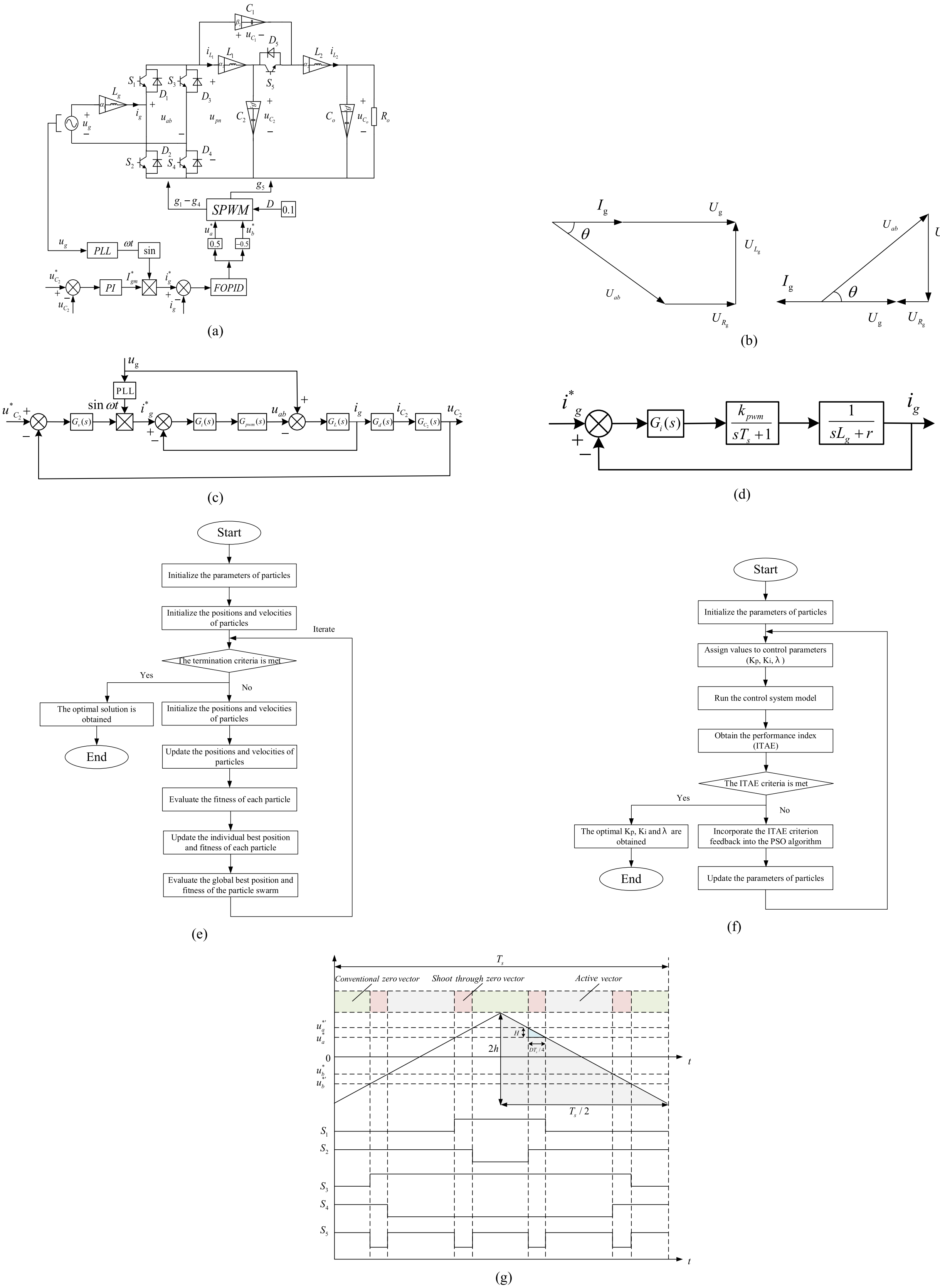

FIGURE 2. **(a) The structure diagram of control system. (b) The vector diagrams of the two possible operation modes on the AC side. (c) The block diagram of double closed-loop control. (d) The block diagram of the simplified current loop. (e) The flow of the PSO algorithm. (f) The flow of the control parameter optimization. (g) The modulation scheme of the single-phase FO-qZSR.**

network. Therefore, we will analyze the impact of FOI and FOC on circuit performance from two aspects.

Under situation I, we assume that the grid side inductor and the dc output capacitor are fractional-order components while the inductors and capacitors in the quasi-Z-source network are integer components. Thus, the grid voltage and grid side current are

$$u_g(t) = \sqrt{2}U_g \sin(\omega t) \quad i_g(t) = \sqrt{2}I_g \sin(\omega t - \theta) \tag{13}$$

where U_g, I_g are the effective values of $u_g(t)$ and $i_g(t)$, respectively. ω is the grid frequency, θ is the phase angle of $i_g(t)$ behinds $u_g(t)$. When $\theta = 0$, the single-phase FO-qZSR operates with positive resistive characteristics. When $\theta = \pi/2$, the single-phase FO-qZSR operates with inductive characteristics. When θ = -π, the single-phase FO-qZSR operates with negative resistive characteristics. When θ = -$\pi/2$, the single-phase FO-qZSR operates with capacitive characteristics.

According to the formula (1) and (13), the voltage of grid side FOI can be derived as

$$u_{L_g}(t) = \sqrt{2}\omega^{\alpha_1} L_g I_g \sin(\omega t - \theta + \pi\alpha_1/2) \tag{14}$$

where α_1 is the order of the grid side inductor.

Under the premise of ignoring the input resistance, and based on the kirchhoff's voltage law, $u_{ab}(t)$ can be expressed as

$$\begin{aligned} u_{ab}(t) = u_g(t) - u_{L_g}(t) = \sqrt{2}U_g \sin(\omega t) \\ - \sqrt{2}\omega^{\alpha_1} L_g I_g \sin(\omega t - \theta + \pi\alpha_1/2) \end{aligned} \tag{15}$$

By assuming $u_{ab}(t)$ in the following

$$u_{ab}(t) = \sqrt{2}U_{ab} \sin(\omega t - \varphi) \tag{16}$$

One can obtain

$$U_{ab} = \sqrt{U_g^2 + (\omega^{\alpha_1} L_g I_g)^2 - 2\omega^{\alpha_1} U_g L_g I_g \cos(-\theta + \pi\alpha_1/2)} \tag{17}$$

$$\varphi = -\arctan \frac{\omega^{\alpha_1} L_g I_g \sin(-\theta + \pi\alpha_1/2)}{Ug - \omega^{\alpha_1} L_g I_g \cos(-\theta + \pi\alpha_1/2)} \tag{18}$$

Based on (17) and (18), we can obtain the variation diagrams as shown in Fig. 3, which indicate the changing tendency of U_{ab} and φ with α_1 and θ, respectively. From Fig. 3(a), one can observe that the influence of order α_1 on U_{ab} is small when $0 < \alpha_1 < 1$, and U_{ab} will be increased along with α_1 increases. Besides, when $\theta = k_1\pi$ ($k_1 \in$ Z), the impact effect is the most significant. While, the influence is minimal when $\theta = \mathrm{k}_2\pi/2$ ($\mathrm{k}_2 \in$Z). From Fig. 3(b), it can be found the influence effect of α_1 on φ is small when $0 < \alpha_1 < 1$, and φ is increased along with α_1 increases. Besides, the influence is biggest when $\theta = k_2\pi/2$ ($k_2 \in$ Z) and the influence is minimal when $\theta = k_1\pi$ ($k_1 \in$ Z). Due to the power factor correction, the phase angle θ of $i_g(t)$ behinds $u_g(t)$ will be zero. Therefore, we will assume $\theta = 0$ in the following analysis. Fig. 3(c) shows variation tendency curve of u_{ab} with α_1 during some periods when $\theta = 0$. It can be seen the amplitude of u_{ab} increases along with α_1 increases.

According to (13), the power supplied by the ac power grid can be obtained as

$$\begin{aligned} p_g(t) = u_g(t)i_g(t) = 2U_g I_g \sin(\omega t)\sin(\omega t - \theta) \\ = U_g I_g[\cos\theta - \cos(2\omega t - \theta)] \end{aligned} \tag{19}$$

Based on (13) and (14), the power of the grid side FOI can be expressed by

$$\begin{aligned} p_{L_g}(t) = u_{L_g}(t)i_g(t) = 2\omega^{\alpha_1} L_g I_g^2 \sin(\omega t + \pi\alpha_1/2)\sin(\omega t - \theta) \\ = \omega^{\alpha_1} L_g I_g^2[\cos(\pi\alpha_1/2) + \cos(2\omega t - \theta + \pi\alpha_1/2)] \end{aligned} \tag{20}$$

Hence, the grid side input power can be obtained as

$$\begin{aligned} p_{in}(t) &= p_g(t) - p_{L_g}(t) \\ &= U_g I_g[\cos\theta - \cos(2\omega t - \theta)] + \omega^{\alpha_1} L_g I_g^2 \\ &\quad [-\cos(\pi\alpha_1/2) + \cos(2\omega t - \theta + \pi\alpha_1/2)] \\ &= [U_g I_g \cos\theta - \omega^{\alpha_1} L_g I_g^2 \cos(\pi\alpha_1/2)] \\ &\quad + [-U_g I_g \cos(2\omega t - \theta) + \omega^{\alpha_1} L_g I_g^2 \cos(2\omega t \\ &\quad - \theta + \pi\alpha_1/2)] \\ &= p_{\mathrm{in\_dc}} + p_{\mathrm{in\_ac}}(t) \end{aligned} \tag{21}$$

where p_{in_dc} is the DC component, and $p_{in\_ac}(t)$ is the ac component of the grid side input power. As can been in Fig. 3(d) and (e), the variation diagrams of these two components when $\theta = 0$. From Fig. 3(d), it can be seen that the amplitude of $p_{in\_ac}(t)$ increases along with α_1 increases. As shown in Fig. 3(e), one can find that p_{in_dc} increases along with α_1 increases.

For the dc side output power, it can be expressed by

$$\begin{aligned} p_{out}(t) &= u_{out}(t)i_{out}(t) \\ &= [u_{out\_dc} + u_{out\_ac}(t)][i_{out\_dc} + i_{out\_ac}(t)] \\ &= u_{out\_dc}i_{out\_dc} + u_{out\_dc}C_o\frac{d^{\beta_1}u_{C_o}}{dt^{\beta_1}} \\ &\quad + i_{out\_dc}u_{out\_ac}(t) + u_{out\_dc}(t)i_{out\_ac}(t) \end{aligned} \tag{22}$$

where $u_{out}(t)$ and $i_{out}(t)$ are the output voltage and the output current, u_{out_dc} and i_{out_dc} are the dc components of $u_{out}(t)$ and $i_{out}(t)$, respectively. $u_{out\_ac}(t)$ and $i_{out\_ac}(t)$ are the ac components of $u_{out}(t)$ and $i_{out}(t)$, β_1 is the order of the output FOC.

Based on (22) and ignoring the high order infinitely small quantities, the dc side output power is

$$\begin{aligned} p_{out}(t) &= u_{out\_dc}i_{out\_dc} + u_{out\_dc}C_o\frac{d^{\beta_1}u_{C_o}}{dt^{\beta_1}} \\ &= p_{out\_dc} + p_{out\_ac}(t) \end{aligned} \tag{23}$$

where p_{out_dc} is the dc component, and $p_{out\_ac}(t)$ is the ac component of the dc side output power.

According to the power balance between input and output side, based on (21)-(23) and ignoring the loss of the rectifier,

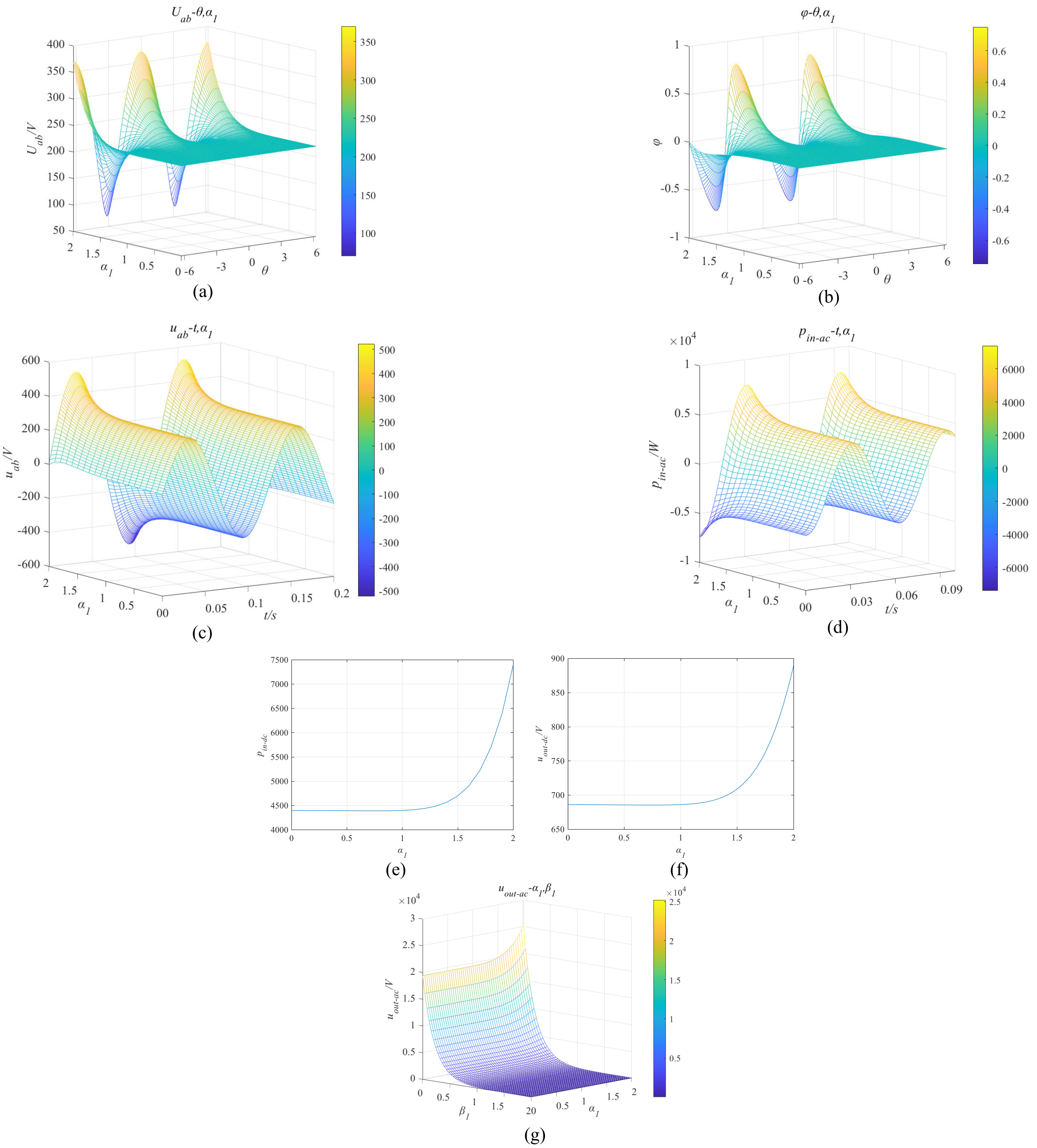

FIGURE 3. The change diagrams. (a) U_{ab} versus θ-α_1 plane. (b) φ versus θ-α_1 plane. (c) u_{ab} versus t-α_1 plane. (d) p_{in_dc} versus α_1. (e) $p_{in\_ac}(t)$ versus t-α_1 plane. (f) u_{out_dc} versus α_1. (g) $u_{out\_ac}(t)$ versus β_1-α_1 plane.

u_{out_dc} and the amplitude of $u_{out\_ac}(t)$ can be derived as

$$u_{out\_dc} = \sqrt{R_o U_g I_g \cos\theta - R_o \omega^{\alpha_1} L_g I_g^2 \cos(\pi\alpha_1/2)} \tag{24}$$

$$u_{out\_acm} = \frac{\sqrt{(U_g I_g)^2 + (\omega^{\alpha_1} L_g I_g)^2 + 2\omega^{\alpha_1} U_g L_g I_g^3 \cos(\pi\alpha_1/2 - \theta)}}{C_o (2\omega)^{\beta_1} u_{out\_dc}} \tag{25}$$

where R_o is the load resistance of the rectifier. Fig. 3(f) and (g) shows the variation diagrams of u_{out_dc} and $u_{out\_ac}(t)$ when $\theta = 0$. As shown in Fig. 3(f), one can obtain that u_{out_dc} increases along with α_1 increases. From Fig. 3(g), it can be observed that the amplitude of $u_{out\_ac}(t)$ increases along with α_1 increases, and decreases with β_1 increases. In addition, the influence of order α_1 on the amplitude of u_{out_ac} is small when $1 < \beta_1 < 2$, and the impact effect increases with β_1 decreases. Meanwhile, the influence of β_1 on the amplitude of u_{out_dc} is small when $1 < \beta_1 < 2$.

Under situation II, we assume that the inductors and capacitors in quasi-Z-source network are fractional-order components, while the grid side inductor and the output capacitor are integer-order components.

Then, H-bridge input power is

$$p_{in}(t) = u_{ab}(t) i_g(t) \tag{26}$$

Since the H-bridge is short-circuited when the rectifier is operating in shoot-through state. Thus, the output power of the H-bridge is

$$p_{H\_out}(t) = D \times 0 + (1 - \mathrm{D}) u_{pn}(t) i_{pn}(t) \tag{27}$$

where D is the shoot-through duty cycle, u_{pn} and i_{pn} are the output voltage and current of H-bridge, respectively.

Based on the power balance of the H-bridge and (26)-(27), the following formula can be obtained as

$$i_{pn}(t) = \frac{u_{ab}(t) i_g(t)}{(1 - D) u_{pn}(t)} \tag{28}$$

Due to the power factor correction, assuming that the phase angle θ of $i_g(t)$ behinds $u_g(t)$ is $\theta = 0$. Then, the H-bridge input current is

$$i_g(t) = \sqrt{2} I_g \sin(\omega t) \tag{29}$$

The relationship between $u_{ab}(t)$ and $u_{pn}(t)$ can be expressed as

$$u_{ab}(t) = M \sin(\omega t) u_{pn}(t) \tag{30}$$

where M is the modulation index.

According to (28), (29) and (30), the output current of the H-bridge can be derived as

$$\begin{aligned} i_{pn}(t) &= i_{pn\_dc} + i_{pn\_ac}(t) \\ &= \frac{\sqrt{2} M I_g \sin^2(\omega t)}{(1 - D)} = \frac{\sqrt{2} M I_g [1 - \cos(2\omega t)]}{2(1 - D)} \\ &= \frac{\sqrt{2} M I_g}{2(1 - D)} + \frac{-\sqrt{2} M I_g \cos(2\omega t)}{2(1 - D)} \end{aligned} \tag{31}$$

where i_{pn_dc} and $i_{pn\_ac}(t)$ are dc component and ac component of H-bridge output current.

Based on the operation principle analysis, the fractional-order state-space averaging model can be written as

$$\begin{cases} \dfrac{d^{\alpha_2} \langle i_{L_1} \rangle}{dt^{\alpha_2}} = \dfrac{-\langle u_{c_2} \rangle}{L_1} d + \dfrac{\langle u_{c_1} \rangle}{L_1} (1 - d) \\ \dfrac{d^{\alpha_2} \langle i_{L_2} \rangle}{dt^{\alpha_2}} = \dfrac{-\langle u_{c_1} \rangle - \langle u_{c0} \rangle}{L_2} d + \dfrac{\langle u_{c_2} \rangle - \langle u_{c_o} \rangle}{L_2} (1 - d) \end{cases}$$
$$\begin{cases} \dfrac{d^{\beta_2} \langle u_{C_1} \rangle}{dt^{\beta_2}} = \dfrac{\langle i_{L_2} \rangle}{C_1} d + \dfrac{\langle i_{pn} \rangle - \langle i_{L_1} \rangle}{C_1} (1 - d) \\ \dfrac{d^{\beta_2} \langle u_{C_2} \rangle}{dt^{\beta_2}} = \dfrac{\langle i_{L_1} \rangle}{C_2} d + \dfrac{\langle i_{pn} \rangle - \langle i_{L_2} \rangle}{C_2} (1 - d) \\ \dfrac{d \langle u_{c_o} \rangle}{dt} = \dfrac{\langle i_{L_2} \rangle - \frac{\langle u_{c_o} \rangle}{R}}{C_o} \end{cases} \tag{32}$$

where $< i_{L1} >$, $< i_{L2} >$, $< i_{pn} >$, $< u_{C1} >$, $< u_{C2} >$, $< u_{Co} >$ are the average values of the circuit variables and they can be described by

$$\begin{cases} \langle i_{L_1} \rangle = i_{L_1\_dc} + i_{L_1\_ac}(t) \\ \langle i_{L_2} \rangle = i_{L_2\_dc} + i_{L_2\_ac}(t) \\ \langle i_{pn} \rangle = i_{pn\_dc} + i_{pn\_ac}(t) \end{cases}$$

$$\begin{cases} \langle u_{C_1} \rangle = u_{C_1\_dc} + u_{C_1\_ac}(t) \\ \langle u_{C_2} \rangle = u_{C_2\_dc} + u_{C_2\_ac}(t) \\ d = d\_{dc} + d\_{ac}(t) = D + d\_{ac}(t) \end{cases} \tag{33}$$

where the ac components are much smaller than the dc components.

For the ac components, we can obtain (34), as shown at the bottom of the next page.

Moreover, by assuming in the following

$$\begin{cases} i_{L_1\_ac}(t) = i_{L_1\_acm} \cos(2\omega t) \\ i_{L_2\_ac}(t) = i_{L_2\_acm} \cos(2\omega t) \end{cases}$$
$$\begin{cases} u_{C_1\_ac}(t) = u_{C_1\_acm} \cos(2\omega t) \\ u_{C_2\_ac}(t) = u_{c_2\_acm} \cos(2\omega t) \\ u_{C_o\_ac}(t) = u_{c_o\_acm} \cos(2\omega t) \end{cases} \tag{35}$$

where i_{L1_acm}, i_{L2_acm}, u_{C1_acm}, u_{C2_acm}, u_{Co_acm} are the amplitudes of $i_{L1\_ac}(t)$, $i_{L2\_ac}(t)$, $u_{C1\_ac}(t)$, $u_{C2\_ac}(t)$, $u_{Co\_ac}(t)$, respectively.

Based on $L_1 = L_2 = L$, $C_1 = C_2 = C$, (31), (34) and (35), the expression of i_{L1_acm}, i_{L2_acm}, u_{C1_acm}, u_{C2_acm}, u_{Co_acm} can be derived as (36), shown at the bottom of the next page.

Fig. 4 shows the variation diagrams of i_{L1_acm}, i_{L2_acm}, u_{C1_acm}, u_{C2_acm}, u_{Co_acm} versus β_2-α_2 plane.

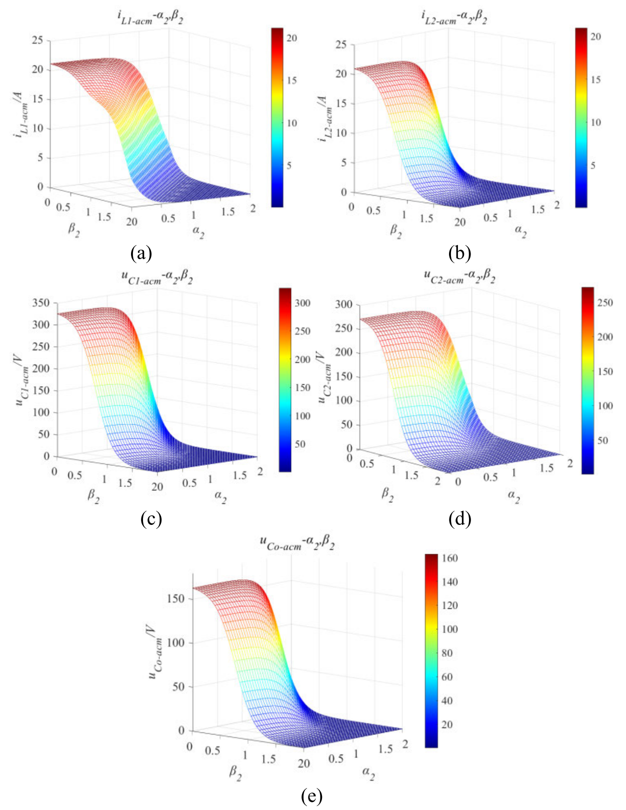

FIGURE 4. The three-dimensional variation diagrams. (a) i_{L1_acm} versus β_2-α_2 plane. (b) i_{L2_acm} versus β_2-α_2 plane. (c) u_{C1_acm} versus β_2-α_2 plane. (d) u_{C2_acm} versus β_2-α_2 plane. (e) u_{Co_acm} versus β_2-α_2 plane.

From Fig. 4(a) and (b), when $0 < \alpha_2 < 1$ and $0 < \beta_2 < 1$, one can obtain that the amplitudes of the ac components i_{L1_acm} and i_{L2_acm} decrease significantly with α_2 and β_2 increasing. From Fig. 4(c) and (d), it can be seen that the amplitudes of the ac components u_{C1_acm} and u_{C2_acm} decrease slowly with α_2 increasing, and decrease significantly with β_2 increasing. Based on the results in Fig. 4(e), it can be observed that the amplitude of the ac component u_{Co_acm} decreases significantly with α_2 and β_2 increasing.

VI. EFFICIENCY ANALYSIS AND ESTIMATION

A. POWER LOSS OF MOSFETs

Power loss of mosfets include the switching loss and conduction loss. They can be estimated by

$$\begin{cases} P_{sw} = \frac{1}{2} I_{ds} V_{ds}(t_{on} + t_{off}) f_s + \frac{1}{2} C_{oss} V_{ds}^2 f_s \\ P_{con} = I_{ds\_rms}^2 r_{on} \end{cases} \tag{37}$$

where I_{ds} and V_{ds} are the average drain-to-source current and withstand voltage of MOSFETs, t_{on} and t_{off} are the turn-on and turn-off time, f_{s} is the switching frequency, C_{oss} is the output capacitor, $I_{\mathrm{ds\_rms}}$ is the rms value of I_{ds} and r_{on} is the on-state resistor.

Based on the above modulation and analysis, the drain-to-source voltage, current and the rms current value of S_1-S_5 can be obtained as

$$\begin{cases} V_{ds,S_1-S_5} = V_{pn} \\ I_{ds,S_1-S_4} = \frac{I_o}{2} \\ I_{ds,S_5} = I_o \\ I_{ds\_rms,S_1-S_4} = \frac{\sqrt{2}}{2} I_{g\_rms} \\ I_{ds\_rms,S_5} = \frac{I_{ds\_rms,S_1-S_4}}{0.9} \end{cases} \tag{38}$$

$$\begin{cases} \frac{d^{\alpha_2} i_{L_1\_ac}(t)}{dt^{\alpha_2}} = \frac{-u_{C_2\_dc} d_{\_ac}(t) - u_{C_2\_ac}(t)D + u_{C_1\_ac}(t) + u_{C_1\_dc} d_{\_ac}(t) - u_{C_1\_ac}(t)D}{L_1} \\ \frac{d^{\alpha_2} i_{L_2\_ac}(t)}{dt^{\alpha_2}} = \frac{-u_{C_1\_dc} d_{\_ac}(t) - u_{C_1\_ac}(t)D + u_{C_2\_ac}(t) - u_{C_o\_ac}(t) - u_{C_2\_dc} d_{\_ac}(t) - u_{C_2\_ac}(t)D}{L_2} \\ \frac{d^{\beta_2} u_{C_1\_ac}(t)}{dt^{\beta_2}} = \frac{i_{L_2\_dc} d_{\_ac}(t) + i_{L_2\_ac}(t)D + i_{pn\_ac}(t) - i_{L_1\_ac}(t) - i_{pn\_dc} d_{\_ac}(t) - i_{pn\_ac}(t)D}{C_1} + \frac{i_{L_1\_dc} d_{\_ac}(t) + i_{L_1\_ac}(t)D}{C_1} \\ \frac{d^{\beta_2} u_{C_2\_ac}(t)}{dt^{\beta_2}} = \frac{i_{L_1\_dc} d_{\_ac}(t) + i_{L_1\_ac}(t)D + i_{pn\_ac}(t) - i_{L_2\_ac}(t) - i_{pn\_dc} d_{\_ac}(t) - i_{pn\_ac}(t)D}{C_2} + \frac{i_{L_2\_dc} d_{\_ac}(t) + i_{L_2\_ac}(t)D}{C_2} \\ \frac{du_{C_o\_ac}(t)}{dt} = \frac{i_{L_2\_ac}(t) - \frac{u_{C_o\_ac}(t)}{R_o}}{C_o} \end{cases} \tag{34}$$

$$\begin{cases} i_{L_1\_acm} = \frac{\sqrt{2} M I_g (2D-1)(C C_o L R_o s^{1+a_2+\beta_2} + C L s^{a_2+\beta_2} + C R_o s^{\beta_2} + C_o R_o s + 1)}{2 \times \begin{bmatrix} (4D^2 - 4D + 2)(C C_o L R_o s^{1+a_2+\beta_2} + C L s^{a_2+\beta_2}) + (4D^2 - 4D + 1)(C_o R_o s + 1) \\ +(2D^2 - 2D + 1) C R_o s^{\beta_2} + (C^2 L s^{a_2+2\beta_2})(C_o L R_o s^{1+a_2} + L s^{a_2} + R_o) \end{bmatrix}} \\ i_{L_2\_acm} = \frac{\sqrt{2} M I_g (2D-1)(C C_o L R_o s^{1+a_2+\beta_2} + C L s^{a_2+\beta_2} + C_o R_o s + 1)}{2 \times \begin{bmatrix} (4D^2 - 4D + 2)(C C_o L R_o s^{1+a_2+\beta_2} + C L s^{a_2+\beta_2}) + (4D^2 - 4D + 1)(C_o R_o s + 1) \\ +(2D^2 - 2D + 1) C R_o s^{\beta_2} + (C^2 L s^{a_2+2\beta_2})(C_o L R_o s^{1+a_2} + L s^{a_2} + R_o) \end{bmatrix}} \\ u_{C_1\_acm} = \frac{\sqrt{2} M I_g (-C C_o L^2 R_o s^{1+2a_2+\beta_2} - C L^2 s^{2a_2+\beta_2} - C L R_o s^{a_2+\beta_2} - C_o L R_o s^{1+\alpha_2} - L s^{\alpha_2} - D R_o)}{2 \times \begin{bmatrix} (4D^2 - 4D + 2)(C C_o L R_o s^{1+a_2+\beta_2} + C L s^{a_2+\beta_2}) + (4D^2 - 4D + 1)(C_o R_o s + 1) \\ +(2D^2 - 2D + 1) C R_o s^{\beta_2} + (C^2 L s^{a_2+2\beta_2})(C_o L R_o s^{1+a_2} + L s^{a_2} + R_o) \end{bmatrix}} \\ u_{C_2\_acm} = \frac{\sqrt{2} M I_g (-C C_o L^2 R_o s^{1+2a_2+\beta_2} - C L^2 s^{2a_2+\beta_2} - C L R_o s^{a_2+\beta_2} - C_o L R_o s^{1+\alpha_2} - L s^{\alpha_2} + D R_o - R_o)}{2 \times \begin{bmatrix} (4D^2 - 4D + 2)(C C_o L R_o s^{1+a_2+\beta_2} + C L s^{a_2+\beta_2}) + (4D^2 - 4D + 1)(C_o R_o s + 1) \\ +(2D^2 - 2D + 1) C R_o s^{\beta_2} + (C^2 L s^{a_2+2\beta_2})(C_o L R_o s^{1+a_2} + L s^{a_2} + R_o) \end{bmatrix}} \\ u_{C_o\_acm} = \frac{\sqrt{2} M I_g (2D-1)(C L R_o s^{a_2+\beta_2} + R_o)}{2 \times \begin{bmatrix} (4D^2 - 4D + 2)(C C_o L R_o s^{1+a_2+\beta_2} + C L s^{a_2+\beta_2}) + (4D^2 - 4D + 1)(C_o R_o s + 1) \\ +(2D^2 - 2D + 1) C R_o s^{\beta_2} + (C^2 L s^{a_2+2\beta_2})(C_o L R_o s^{1+a_2} + L s^{a_2} + R_o) \end{bmatrix}} \end{cases} \tag{36}$$

Therefore, the total switching loss and conduction loss of MOSFETs can be derived as

$$\begin{cases} P_{sw} = 4(\frac{1}{2}I_{ds,S_1-S_4}V_{ds,S_1-S_4}(t_{on}+t_{off})f_{s,S_1-S_4} \\ +\frac{1}{2}C_{oss}V_{ds,S_1-S_4}^2 f_{s,S_1-S_4}) \\ +\frac{1}{2}I_{ds,S_5}V_{ds,S_5}(t_{on}+t_{off})f_{s,,S_5}+\frac{1}{2}C_{oss}V_{ds,S_5}^2 f_{s,,S_5} \\ P_{con} = 4(I_{ds\_rms,S_1-S_4}^2 r_{on}) + I_{ds\_rms,S_5}^2 r_{on} \end{cases} \tag{39}$$

B. POWER LOSS OF INDUCTORS AND CAPACITORS

According to Caputo definition, the Laplace transform of (1) gives the relationship between voltage and current in the complex frequency domain as

$$\begin{cases} u_L(s) = s^{\alpha} L_{\alpha} i_L(s) \\ i_C(s) = s^{\beta} C_{\beta} u_C(s) \end{cases} \tag{40}$$

Based on (40), the impedance expressions for FOI and FOC can be obtained as

$$\begin{cases} Z_L(s) = s^{\alpha} L_{\alpha} \\ Z_C(s) = \frac{1}{s^{\beta} C_{\beta}} \end{cases} \tag{41}$$

Replacing s in (41) with $j\omega$ gives the phase expressions for FOI and FOC as

$$\begin{cases} Z_L(j\omega) = (j\omega)^{\alpha} L_{\alpha} = \omega^{\alpha} L_{\alpha}(\cos(\frac{\pi}{2}\alpha) + j\sin(\frac{\pi}{2}\alpha)) \\ Z_C(j\omega) = \frac{1}{(j\omega)^{\beta} C_{\beta}} = \frac{1}{\omega^{\beta} C_{\beta}}(\cos(\frac{\pi}{2}\beta) - j\sin(\frac{\pi}{2}\beta)) \end{cases} \tag{42}$$

It can be seen from (42) that FOI and FOC contain resistive components. Since the actual integer-order inductors and capacitors contain dc resistance, r_{Lg}, $r_{\mathrm{L1,2}}$, r_{Co} and $r_{\mathrm{C1,2}}$ can be obtained by

$$\begin{cases} r_{L_g} = r_{L_g,FO} + r_{L_g,IO} = \omega^{\alpha_1} L_g \cos(\frac{\pi}{2}\alpha_1) + r_{L_g,IO} \\ r_{L1,2} = r_{L_{1,2},FO} + r_{L_{1,2},IO} = \omega^{\alpha_2} L_{1,2}\cos(\frac{\pi}{2}\alpha_2) + r_{L_{1,2},IO} \\ r_{C_o} = r_{C_o,FO} + r_{C_o,IO} = \frac{1}{\omega^{\beta_1} C_o}\cos(\frac{\pi}{2}\beta_1) + ESR_{C_o,IO} \\ r_{C1,2} = r_{C_{1,2},FO} + r_{C_{1,2},IO} = \frac{1}{\omega^{\beta_2} C_{1,2}}\cos(\frac{\pi}{2}\beta_2) \\ \qquad + ESR_{C_{1,2},IO} \end{cases} \tag{43}$$

The power loss of L_{g}, $L_{1,2}$, C_{o}, $C_{1,2}$ can be derived by

$$\begin{cases} P_{L_g} = I_{L_g\_rms}^2 r_{L_g} \\ P_{L12} = 2P_{L_{1,2}} = 2I_{L_{1,2}\_rms}^2 r_{L1.2} \\ P_{C_o} = I_{C_o\_rms}^2 r_{C_o} \\ P_{C12} = 2P_{C_{1,2}} = 2I_{C_{1,2}\_rms}^2 r_{C1.2} \end{cases} \tag{44}$$

where $I_{\mathrm{Lg\_rms}}$, $I_{\mathrm{L1,2\_rms}}$, $I_{\mathrm{Co\_rms}}$ and $I_{\mathrm{C1,2\_rms}}$ are the rms values of the current of L_{g}, $L_{1,2}$, C_{o}, $C_{1,2}$ respectively. r_{Lg}, $r_{\mathrm{L1,2}}$, r_{Co} and $r_{\mathrm{C1,2}}$ are the resistors of L_{g}, $L_{1,2}$, C_{o}, $C_{1,2}$ respectively. P_{L12} is the total power loss of L_1 and L_2; P_{C12} is the total power loss of C_1 and C_2.

C. POWER EFFICIENCY ESTIMATION

The total power loss of the single-phase fractional-order PWM rectifier can be calculated by

$$P_{total} = P_{sw} + P_{con} + P_{L_g} + P_{L_{12}} + P_{C_o} + P_{C_{12}} \tag{45}$$

Then, the power efficiency of the FO-qZSR rectifier can be estimated by

$$\eta = (P_{in} - P_{total})/P_{in} \times 100\% \tag{46}$$

Based on the above analysis and the parasitic parameters for power loss analysis in Table 2, the detailed power loss in devices and loss distribution percentage when $\alpha_1 = \alpha_2 = \beta_1 = \beta_2 = 1$ are shown in Fig. 5(a) and (b). It can be observed that the total power loss is about 44.9W, and the major power losses come from MOSFETs and inductors, and their corresponding loss distribution percentage are 67% and 30%, respectively.

Moreover, Fig. 5(c) and (d) show the relationship diagram between the order of FOI/FOC and the converter power loss. It can be seen that the power loss increases firstly and then decreases as α_1 or α_2 increasing. And the power loss decreases as β_1 or β_2 increasing.

TABLE 2. Parasitic parameters for power loss analysis.

Parameters	Values
MOSFET S_1-S_5 (GC3M0040120D)	$r_{ds(\max)}$= 68mΩ
MOSFET S_1-S_5 (GC3M0040120D)	C_{oss}=103pF
Parasitic resistance of inductors (L_g, L_1, L_2)	40mΩ
ESR of capacitors (C_1, C_2)	398mΩ
ESR of capacitors (C_o)	800mΩ

VII. SIMULATION VERIFICATION AND ANALYSIS

A. REALIZATION OF FOIs AND FOCs

In order to confirm the above theoretical analysis, the circuit simulation model of single-phase FO-qZSR is built in MATLAB/Simulink platform. Due to there are no FOI and FOC elements in simulink library, we will build them by using integer-order components (e.g., inductor, capacitor or resistor) based on the Oustaloup's approximation method. The principle of the Oustaloup's approximation is to fit the fractional-order operator by using continuous Oustaloup filter. The standard form of Oustaloup filter can be expressed as

$$s^{\gamma} \approx k\prod_{n=1}^{N}\frac{s+\omega_n'}{s+\omega_n}, \gamma > 0 \tag{47}$$

where γ is the order of fractional operator and N is the order of Oustaloup filter. Here, the lower limit of the frequency is defined as ω_b, and the upper limit of the frequency is defined as ω_h. Then, the gain K, the pole ω_n and zero $\omega' \; n$ of the Oustaloup filter can be expressed by

$$K = \omega_h^{\gamma}\omega_n = \omega_b(\frac{\omega_h}{\omega_b})^{\frac{2n-1+\gamma}{2N}} \quad \omega_n' = \omega_b(\frac{\omega_h}{\omega_b})^{\frac{2n-1-\gamma}{2N}} \tag{48}$$

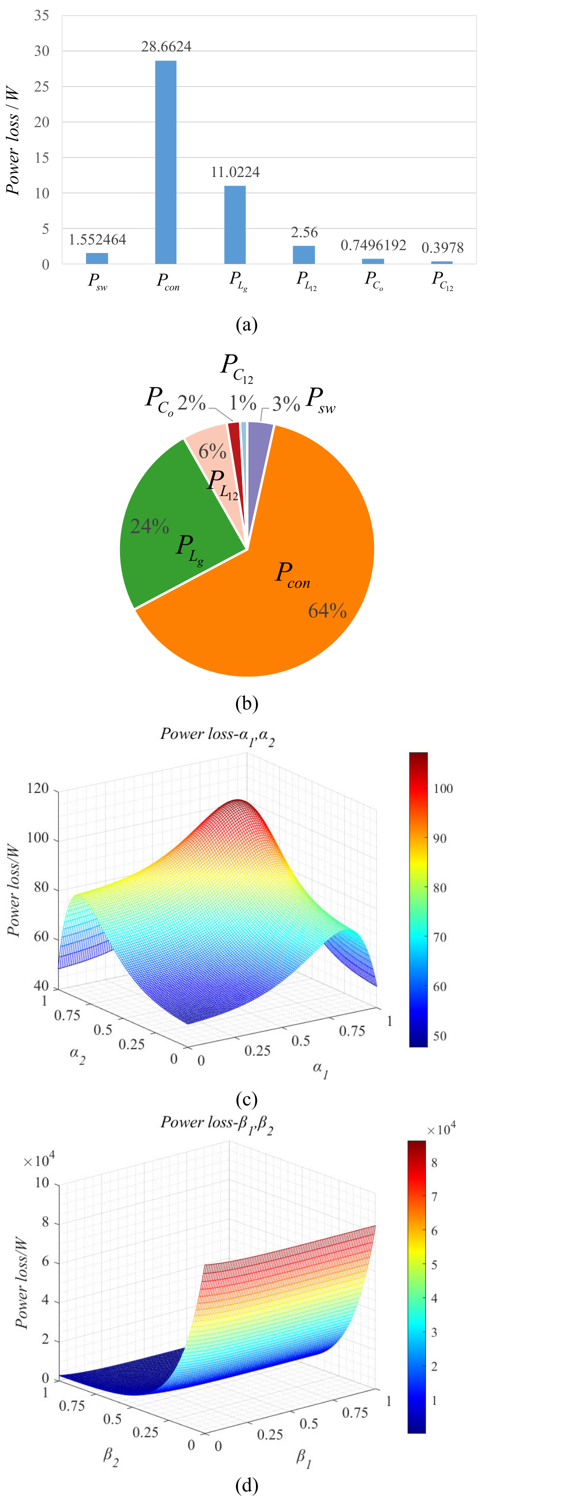

FIGURE 5. **(a) The detailed power loss in devices. (b) The loss distribution percentage. (c) The effect of α_1 and α_2 on power loss. (d) The effect of β_1 and β_2 on power loss.**

ω_b and ω_h are the upper and lower limits of the frequency band of interest respectively, and the switching frequency of the single-phase FO-qZSR is 10kHz in this paper. In general, an nth-order filter works well if the difference between the upper and lower limits of the frequency band is n tenths of an octave. Thus, we assume $N = 8, \omega_b = 1\times10^{-2}, \omega_h = 1\times10^{6}$ when build the AC side inductor and the output capacitor. Besides, we assume $N = 10$, $\omega_b = 1 \times 10^{-2}$, $\omega_h = 1 \times 10^{8}$ when build inductors and capacitors of the quasi-Z-source nrtwork. Then, we can build the FOI and FOC elements based on Oustaloup's approximation method. For example, when $L_g = 3\text{mH}, \alpha_1 = 0.85$, the bode diagram of the FOI's approximated model can be obtained as shown in Fig. 6(a). When $C_o = 330\mu\text{F}$, $\beta_1 = 0.85$, the bode diagram of the FOC's approximated model can be obtained as shown in Fig. 6(b). It can be seen that the difference between the eighth-order fitting curve of the Oustaloup filter and the theoretical curve is not significant in the frequency range of 10Hz to 100kHz.

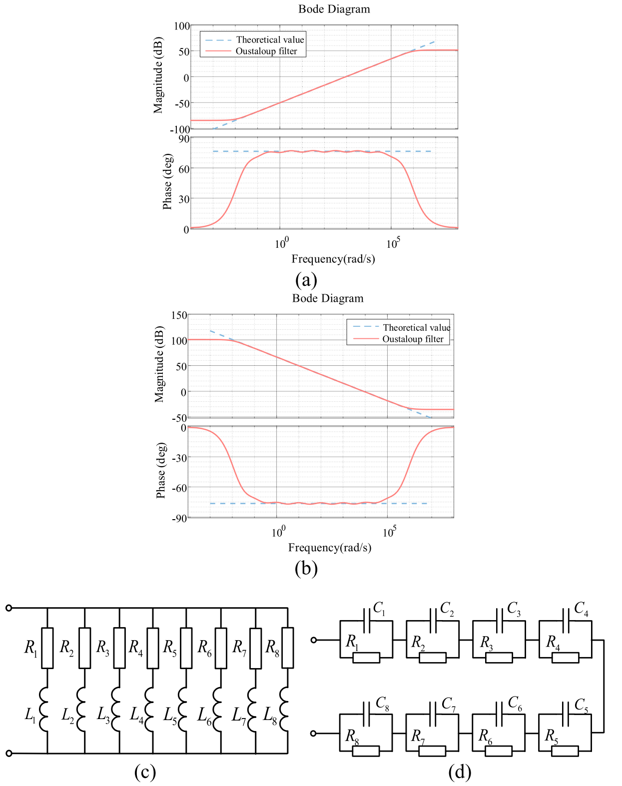

FIGURE 6. **(a) Comparison between the Oustaloup filter's eighth-order fitting curve and theoretical curve for FOI. (b) Comparison between the Oustaloup filter's eighth-order fitting curve and theoretical curve for FOC. (c) Approximate circuit models of the FOI. (d) Approximate circuit model of the FOC.**

Besides, the approximate circuit models of FOI and FOC are shown in Fig. 6(c) and (d). The specific parameters of the integer-order elements for building the fractional-order components are listed in Table. 3 and Table. 4, respectively. In addition, the main parameters of the single-phase FO-qZSR are tabulated in Table. 5. And the adopted FO-$\text{PI}^{\lambda}\text{D}^{\mu}$ controller is constructed by using the high precision Oustaloup derivative operator in FOTF toolbox.

B. SIMULATIONS RESULTS AND ANALYSIS

1) SIMULATION SCENARIO I

The inductors and capacitors of the fractional-order quasi-Z-source rectifier are all integer order components. We set

TABLE 3. The parameters of integer components for building the FOIs.

FOI	3mH					17mH			
α_1	0.85		0.92		α_2	0.8		0.9	
i	$R_i(\Omega)$	L_i(mH)	$R_i(\Omega)$	L_i(mH)	i	$R_i(\Omega)$	L_i(mH)	$R_i(\Omega)$	L_i(mH)
1	205.479	1.728	792.113	7.226	1	20.830k	1.654	184.104k	16.403
2	26.509	2.232	86.573	7.896	2	3.027k	2.405	21.135k	18.842
3	3.705	3.116	10.303	9.394	3	473.693	3.762	2.634k	23.474
4	0.523	4.397	1.240	11.311	4	75.396	5.991	331.464	29.537
5	73.921m	6.221	0.149	13.542	5	11.907	9.457	41.760	37.228
6	10.387m	8.739	17.827m	16.269	6	1.889	15.001	5.257	46.849
7	1.374m	11.562	1.976m	18.014	7	0.299	23.772	0.659	58.778
8	0.063m	5.303	0.045m	4.055	8	47.159m	37.467	82.669m	73.682
					9	7.072m	56.169	9.681m	86.259
					10	0.460	36.515	0.278m	24.794

TABLE 4. The parameters of integer components for building the FOCs.

FOC	330μF					1.2mF			
β_1	0.85		0.92		β_2	0.8		0.9	
i	$R_i(\Omega)$	C_i(μF)	$R_i(\Omega)$	C_i(μF)	i	$R_i(\Omega)$	C_i(μF)	$R_i(\Omega)$	C_i(mF)
1	0.044	192	11.481m	795	*1*	0.680m	116.844	0.077m	1.156
2	0.343	245	0.105	868	2	4.685m	169.554	0.679m	1.332
3	2.457	342	0.883	1.033k	3	29.832m	266.238	5.373m	1.659
4	17.364	484	7.328	1.245k	4	0.188	422.148	42.806m	2.082
5	122.865	685	61.182	1.490k	5	1.190	667.355	0.339	2.630
6	876.859	960	510.202	1.789k	6	7.499	1.059k	2.697	3.304
7	6.613k	1.272k	4.599k	1.983k	7	47.371	1.677k	21.463	4.153
8	144.239k	583	204.491k	446	8	300.216	2.646k	171.270	5.204
					9	2.003k	3.965k	1.466k	6.079
					10	30.820k	2.577k	50.932k	1.750

TABLE 5. The main parameters of the single-phase FO-qZSR.

Parameters	Symbols	Values
The power grid voltage	u_g	220V
The grid voltage frequency	f	50Hz
The switching frequency	f_s	10kHz
The grid side inductor	L_g	3mH
The quasi-Z-source network inductor	L_1=L_2	17mH
The quasi-Z-source network capacitor	C_1=C_2	1.2mF
The shoot through duty cycle	D	0.1
The output capacitor	C_o	330μH
The load resistor	R_o	40Ω

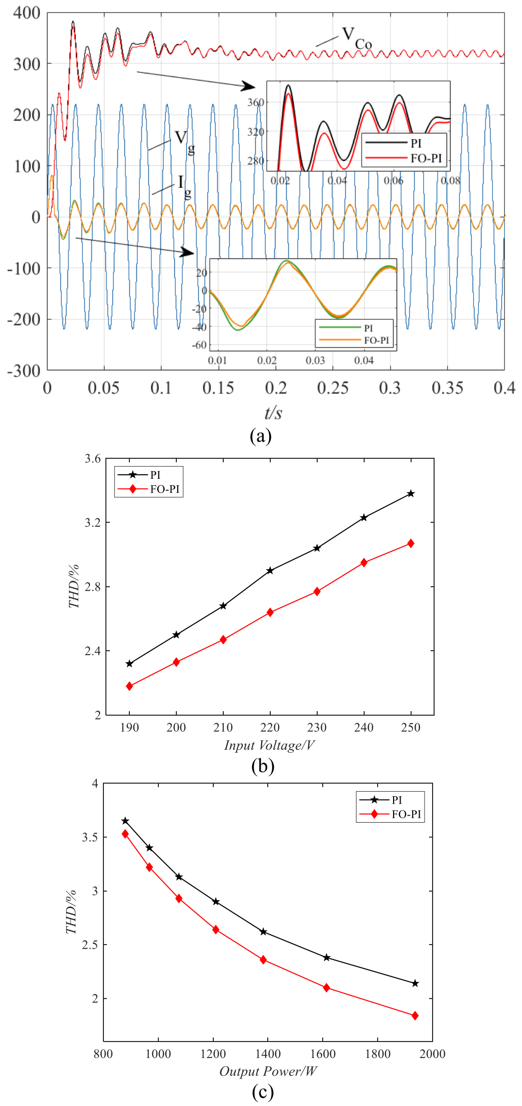

FIGURE 7. (a) AC side voltage, current and DC side output voltage under PI and FO-PI$^{\lambda}$ control. (c) AC side input current THD comparison under various input voltage. (d) AC side input current THD comparison under various output power.

TABLE 6. Parameter values of PI and FO-PI$^{\lambda}$ controllers.

Controller	K_p	K_i	λ
PI	0.08	5.00	1
FO-PI$^{\lambda}$	0.11	5.20	-0.99

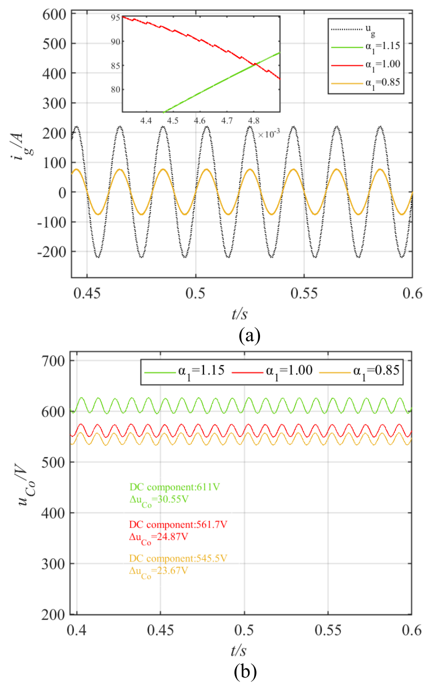

FIGURE 8. Simulation waveforms when $I_{gm}^{*} = 75$A, $\beta_1 = 1.00$, $\alpha_1 = 1.15$, $\alpha_1 = 1.00$, $\alpha_1 = 0.85$. (a) Grid side input current. (c) Output voltage of u_{Co}.

the capacitor voltage reference value is $u_{C2}^{*} = 360$V and the shoot through duty $D = 0.1$. The dual closed-loop controller is used to realize that i_g tracks u_g in phase and u_{C2} tracks u_{C2}^{*}. Besides, the classic PI and FO-PI$^{\lambda}$ controller are used in the current loop, respectively. The parameter values of controllers are listed in Table 6. Fig. 7(a) shows the AC side voltage, current and output voltage waveforms of the rectifier under classic PI and FO-PI$^{\lambda}$ control algorithms, respectively. It can be found that the waveform of AC side current is sinusoidal, the unity power factor can be unitized and the output voltage can stay be stable maintained at 320V, which is consistent with the calculation results from formula (6) when $u_{C2} = 360$V, $D = 0.1$. However, one can find that under FO-PI$^{\lambda}$ control, the system has less overshoot and better dynamic characteristics than that of the classic PI control.

Fig. 7(b) shows the comparison of AC side current THD under different input voltages based on these two different control algorithms. Fig. 7(c) shows the AC side current THD comparison under different output power condition. It can be seen that the AC side current THD value under FO-PI$^{\lambda}$ control is less than that of the classical PI control. Therefore, the FO-PI$^{\lambda}$ control is better in harmonic compensation and reduces the more harmonic pollution on AC side. The power quality is improved by using FO-PI$^{\lambda}$ control algorithm for the qZSR rectifier.

2) SIMULATION SCENARIO II

The inductors and capacitors of quasi-Z-source network are integer-order components ($\alpha_2 = 1.0$, $\beta_2 = 1.0$). In order to obtain simulation results when the order of grid side inductor α_1 varies and analyze the impact on operating characteristics of FO-qZSR. We set three simulation conditions for α_1, which are $\alpha_1 = 1.15$, $\alpha_1 = 1.00$, $\alpha_1 = 0.85$. Here, we set $\beta_1 = 1.00$, $I_{gm}^{*} = 75$A, $D = 0.1$. The grid side input current i_g tracks u_g in phase and tracks I_{gm}^{*} in amplitude. The capacitor voltage u_{C2} is open-loop controlled. From Fig. 8(a), it can be found that the current pulsation decreases with α_1 increasing. As shown in Fig. 8(b), the DC component of u_{Co} is 545.5V when $\alpha_1 = 0.85$, $u_{Co} = 561.7$V when $\alpha_1 = 1.00$ and

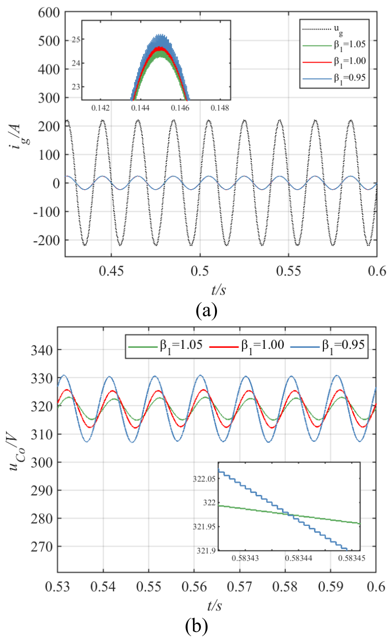

FIGURE 9. Simulation waveforms when $u_{C2}^{*} = 360V$, $\alpha_1 = 1.00$, $\beta_1 = 1.05$, $\beta_1 = 1.00$, $\beta_1 = 0.95$. (a) Grid side input current. (b) Voltage of u_{Co}.

$u_{Co} = 611V$ when $\alpha_1 = 1.15$. As shown in Fig. 8(b), the voltage ripple of u_{Co} is 23.67V when $\alpha_1 = 0.85$, $\Delta u_{Co} = 24.87V$ when $\alpha_1 = 1.00$ and $\Delta u_{Co} = 30.55V$ when $\alpha_1 = 1.15$. It can be seen that the DC component and the voltage ripple of u_{Co} increase with α_1 increasing. Obviously, these simulation results are fit well with the changing trend in Fig. 3.

Similarly, in order to obtain simulation results when the order of output capacitor β_1 varies and analyze the impact on operating characteristics of FO-qZSR. We set three simulation conditions for β_1, which are $\beta_1 = 1.05$, $\beta_1 = 1.00$, $\beta_1 = 0.95$. Here, we set $\alpha_1 = 1.00$, $u_{C2}^{*} = 360V$, $D = 0.1$. Moreover, we use the dual closed-loop controller, which contains a fractional-order proportional-integral-derivative, to control the single-phase fractional-order quasi-Z-source rectifier. As shown in Fig. 9(a), the grid side input current i_g tracks u_g in phase. The amplitude of i_g is 24.7A when $\beta_1 = 1.05$, $i_g = 24.5A$ when $\beta_1 = 1.00$ and $i_g = 24.3A$ when $\beta_1 = 0.95$. It can be obtained that the amplitude of i_g increases with β_1 decreasing. From Fig. 9(b), it can be obtained that the steady-state values of u_{Co} are all around 320V when $\beta_1 = 1.05$, $\beta_1 = 1.00$ and $\beta_1 = 0.95$. Besides, the voltage ripple of u_{Co} is 7.3V when $\beta_1 = 1.05$, $\Delta u_{Co} = 13.8V$ when $\beta_1 = 1.00$ and $\Delta u_{Co} = 24.1V$ when $\beta_1 = 0.95$ according to Fig. 9(b). It can be found that the voltage ripple of u_{Co} increases with β_1 decreasing. Besides, Fig. 9(b) shows the pulsation of u_{Co} when $\beta_1 = 1.05$ and $\beta_1 = 0.95$, respectively. One can clearly find that the pulsation of u_{Co} decreases with β_1 increasing. Therefore, the above simulation results are all in consistent with calculation results in Fig. 3(g).

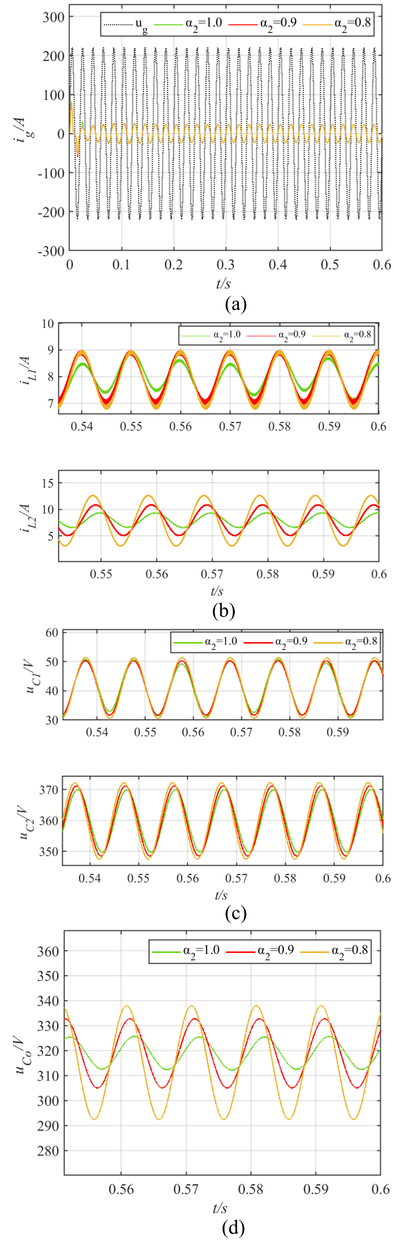

FIGURE 10. Simulation waveforms when $u_{C2}^{*} = 360V$, $\beta_2 = 1.0$, $\alpha_2 = 1.0$, $\alpha_2 = 0.9$, $\alpha_2 = 0.8$. (a) Grid side current. (b) Current of L_1 and L_2. (c) Voltage of C_1 and C_2. (d) Voltage of C_o.

3) SIMULATION SCENARIO III

In this section, the grid side inductor and output capacitor are integer-order components ($\alpha_1 = 1.00$, $\beta_1 = 1.00$). And a dual closed-loop controller, which contains a FO-PI$^{\lambda}$D$^{\mu}$, are utilized to control the single-phase fractional-order quasi-Z-source rectifier. According to the inductor order of the quasi-Z-source network, we set $\alpha_2 = 1.0$, $\alpha_2 = 0.9$, $\alpha_2 = 0.8$, $u_{c2}^{*} = 360V$, $\beta_2 = 1.0$, $D = 0.1$. The corresponding simulation results are shown in Fig. 10. From Fig. 10(a), we can see that the phase of the grid side current i_g follows the phase of grid voltage u_g. In Fig. 10(b), it can be seen that the steady state values of i_{L1} and i_{L2} are 8A. Besides, one can find

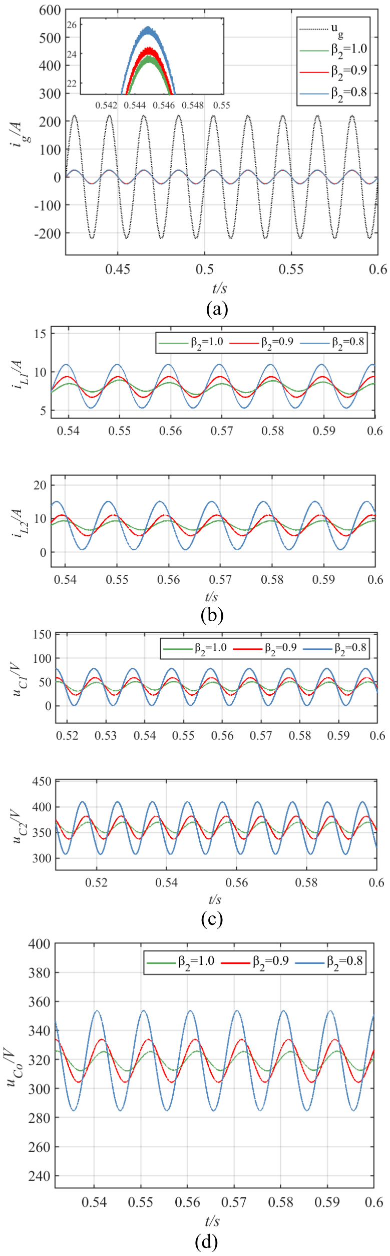

FIGURE 11. Simulation waveforms when $u_{C2}^{*} = 360$V, $\alpha_2 = 1.0$, $\beta_2 = 1.0$, $\beta_2 = 0.9$, $\beta_2 = 0.8$. (a) Grid side current. (b) Inductor current i_{L1}. (c) Inductor current i_{L2}. (d) Capacitor voltage of u_{C1}. (e) Capacitor voltage of u_{C2}. (f) Output voltage of u_{Co}.

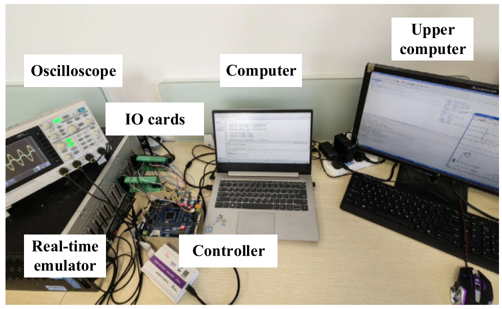

FIGURE 12. The experimental hardware test bench.

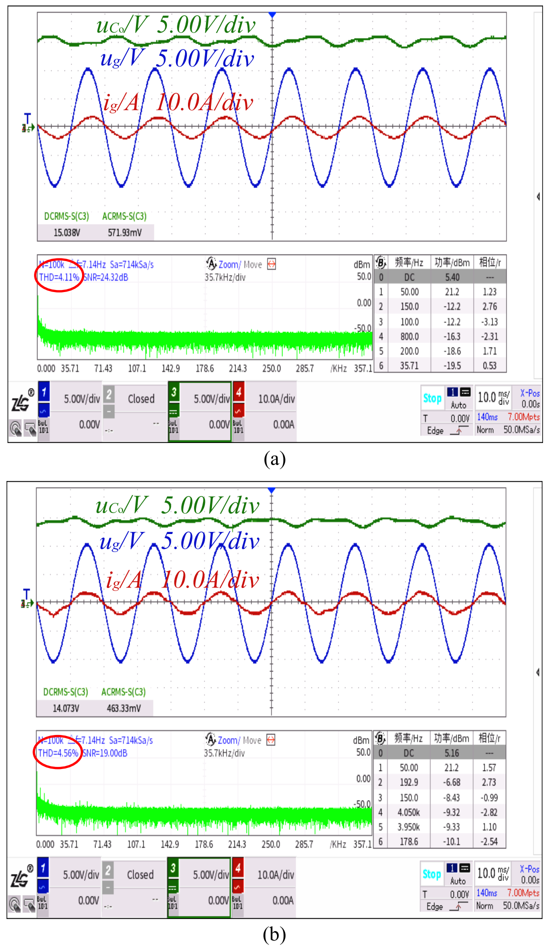

FIGURE 13. Experimental waveforms when (a) $\alpha_1 = 1.15$. (b) $\alpha_1 = 1.00$.

that the current ripple of i_{L1} is 1.18A when $\alpha_2 = 1.0$, $\Delta i_{L1} = 1.91$A when $\alpha_2 = 0.9$ and $\Delta i_{L1} = 2.18$A when $\alpha_2 = 0.8$. The current ripple of i_{L2} is 2.73A when $\alpha_2 = 1.0$, $\Delta i_{L2} = 5.91$A when $\alpha_2 = 0.9$ and $\Delta i_{L2} = 9.55$A when $\alpha_2 = 0.8$. In Fig. 10(c), it can be seen that the steady state value of u_{C1} is 40V and the steady state value of u_{C2} is 360V. Besides, the voltage ripple of u_{C1} is 16.67V when $\alpha_2 = 1.0$, $\Delta u_{C1} = 18.33$V when $\alpha_2 = 0.9$ and $\Delta u_{C1} = 20.00$V when $\alpha_2 = 0.8$. The voltage ripple of u_{C2} is 20.00V when $\alpha_2 = 1.0$, $\Delta u_{C2} = 22.08$V when $\alpha_2 = 0.9$ and $\Delta u_{C2} = 24.17$V when $\alpha_2 = 0.8$. In Fig. 10(d), one can find that the steady state value of u_{Co} is 320V. Besides, the voltage ripple of u_{Co} is 13.02V when $\alpha_2 = 1.0$, $\Delta u_{Co} = 26.50$V when $\alpha_2 = 0.9$ and $\Delta u_{Co} = 45$V when $\alpha_2 = 0.8$. Therefore, it can be seen from Fig. 10 that the ripple of i_{L1}, i_{L2}, u_{C1}, u_{C2} and u_{Co} increase with α_2 decreasing. These simulation results are basically consistent with the changing trend in Fig. 4(a)~(e).

Similarly, in order to study the influence of capacitor order in qZS-network on the system output waveforms. We set $\beta_2 = 1.0$, $\beta_2 = 0.9$, $\beta_2 = 0.8$, respectively. While, $u_{C2}^{*} = 360$V, $\alpha_2 = 1.0$. The simulation results are present in Fig. 11.

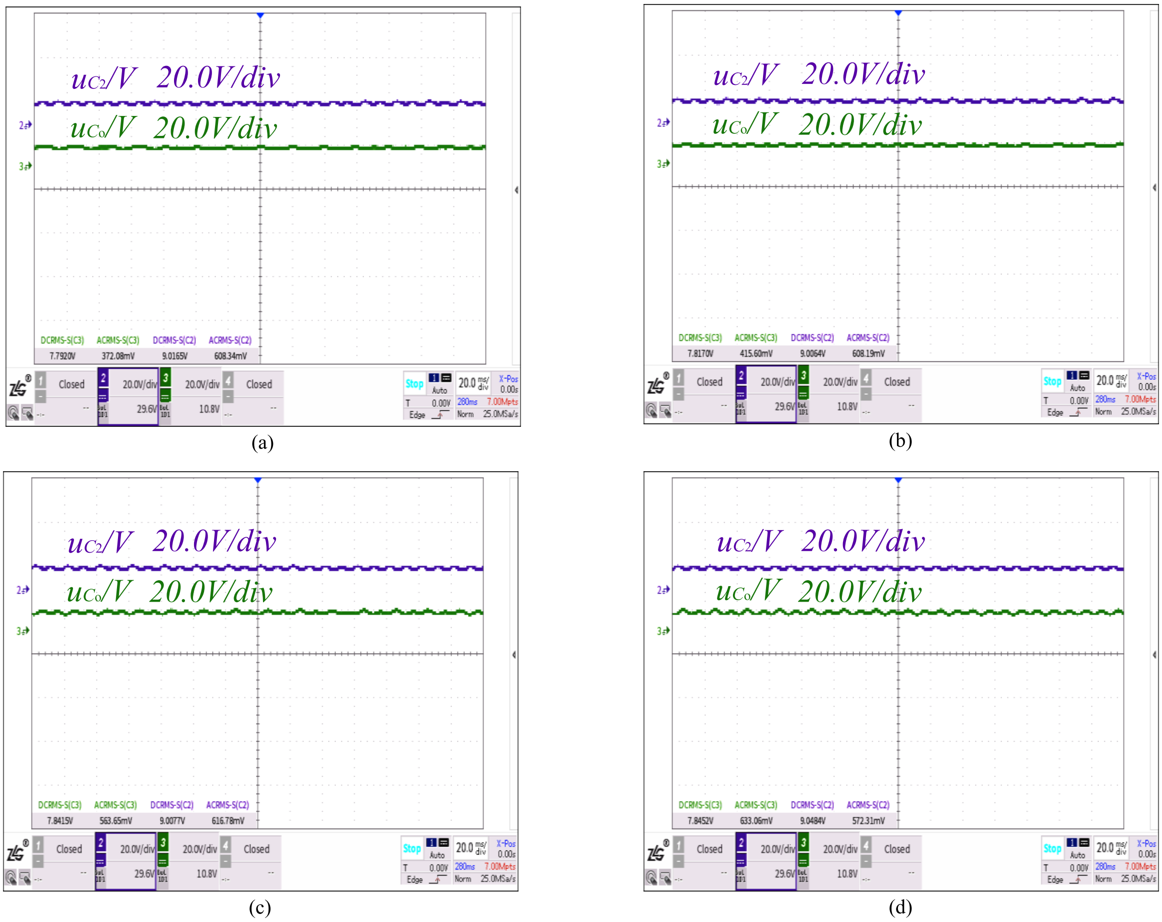

FIGURE 14. Experimental waveforms when (a) $\beta_1 = 1.05$. (b) $\beta_1 = 1.00$. (c) $\beta_1 = 0.95$. (d) $\beta_1 = 0.90$.

From Fig. 11(a), we can see that the grid side current i_g is in phase with the ac input voltage u_g. The amplitude of i_g is 23.8A when $\beta_2 = 1.0$, it is 24.2A and 25.5A when $\beta_2 = 0.9$ and $\beta_2 = 0.8$, respectively. It can be seen that the amplitude of i_g increase with β_2 decreasing. From Fig. 11(b), one can find that the steady state values of i_{L1} and i_{L2} are 8A. Additionally, the ripple of i_{L1} is 1.15A when $\beta_2 = 1.0$, it is 2.69A and 5.77A when $\beta_2 = 0.9$ and $\beta_2 = 0.8$, respectively. The ripple of i_{L2} is 2.73A when $\beta_2 = 1.0$, $\Delta i_{L2} = 6.36$A when $\beta_2 = 0.9$ and $\Delta i_{L2} = 15.45$A when $\beta_2 = 0.8$. In Fig. 11(c), it can be seen that the steady state value of u_{C1} is almost 40V and the steady state value of u_{C2} is almost 360V. In addition, the ripple of u_{C1} is 16.07V when $\beta_2 = 1.0$, it is 35.71V and 76.79V when $\beta_2 = 0.9$ and $\beta_2 = 0.8$, respectively. The ripple of u_{C2} is 20.00V when $\beta_2 = 1.0$, it is 43.33V when $\beta_2 = 0.9$ and it is 100V when $\beta_2 = 0.8$. In Fig. 11(d), one can find that the steady state value of u_{Co} is around 320V. Besides, the voltage ripple of u_{Co} is 12.12V when $\beta_2 = 1.0$, it is 29.09V when $\beta_2 = 0.9$ and $\Delta u_{Co} = 70.30$V when $\beta_2 = 0.8$. It can be found that the ripples of i_{L1}, i_{L2}, u_{C1}, u_{C2} and u_{Co} increase significantly as the capacitor order β_2 decreases, which are in accordance with the changing trend in Fig. 4(a)∼(e).

VIII. EXPERIMENTAL RESULTS VALIDATION AND ANALYSIS

Fractional-order inductors and capacitors are difficult to realize physically due to the need for small and precise resistances. Thanks to the development of semi-physical hardware-in-loop real-time simulation technology, an accurate modeling of single-phase FO-qZSR can be performed based on RT-LAB platform. Fig. 12 shows the experimental hardware bench. The control chip is TMS320F28335. The parameters used in the experiment are identical to the simulation parameters summarized in Table 5. The results of the experiment corresponding to the simulations are shown in the following.

Fig. 13 shows the influence of AC side inductor order α_1 on the experimental waveforms of the single-phase FO-qZSR when $\alpha_1 = 1.00$ and $\alpha_1 = 1.15$, respectively. According to the lower labeling in the figure, the DC and ripple components of the output voltage u_{Co} can be obtained. Since the oscilloscope shrinks the value by a factor of 40, it can be calculated that the rms value of DC component is 15.038*40 = 601.52V when $\alpha_1 = 1.15$ and it is 14.073*40 = 562.92V when $\alpha_1 = 1.00$. For the same reason, the rms value of ripple component of the output voltage is 571.93mV∗40 = 22.8772V when

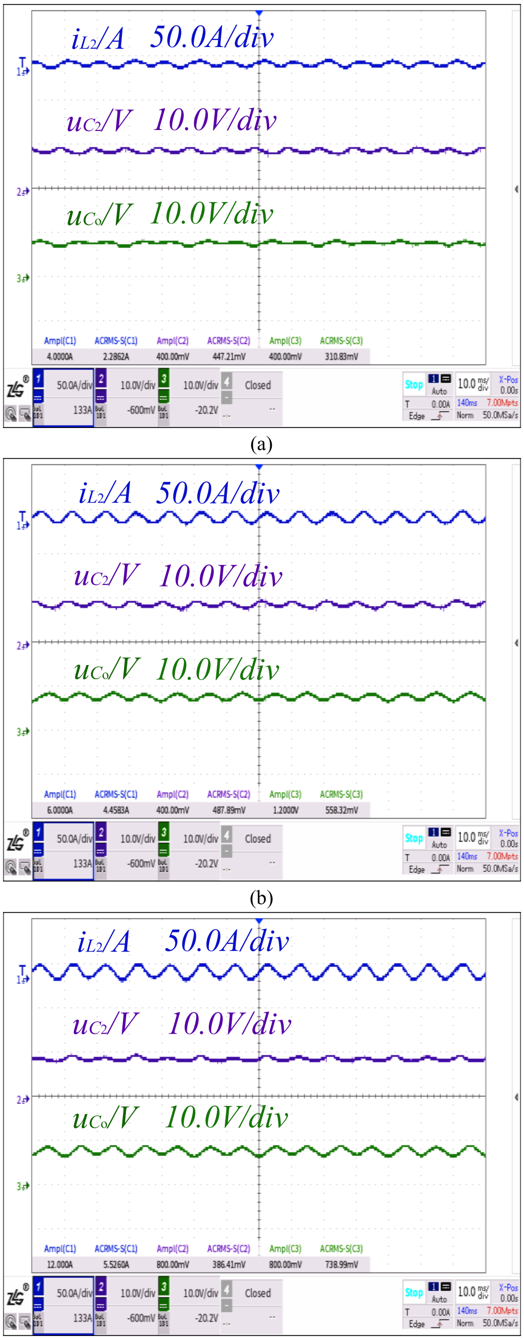

FIGURE 15. Experimental waveforms when (a) $\alpha_2 = 1.0$. (b) $\alpha_2 = 0.95$. (c) $\alpha_2 = 0.9$.

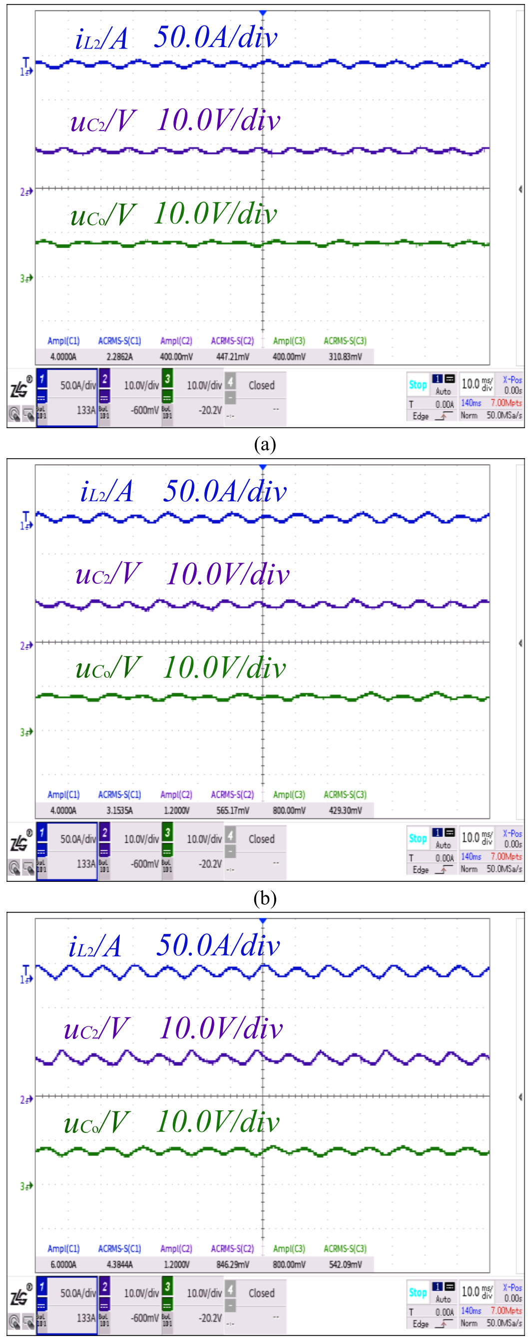

FIGURE 16. Experimental waveforms when (a) $\beta_2 = 1.0$. (b) $\beta_2 = 0.95$. (c) $\beta_2 = 0.9$.

$\alpha_1 = 1.15$ and it is 463.33mV*40 = 18.5332V when $\alpha_1 = 1.00$. It can be seen that the experimental results and the simulation results in *Simulation scenario II* are essentially the same. And it verifies that the DC and ripple components decrease with the inductor order α_1 decreasing. The above conclusions are consistent with the theoretical analysis and simulation results. Besides, the measured THD value of AC side current is 4.11% when $\alpha_1 = 1.15$, and it is 4.56% when $\alpha_1 = 1.00$ by performing FFT analysis of the current. This indicates that the power factor of this FO-qZSR is approximated as 1.

Fig. 14 shows the influence of output capacitor order β_1 on the experimental waveforms of the capacitor voltage u_{Co}. From the lower labeling in the figure, the ripple of the output voltage u_{Co} can be obtained. Since the oscilloscope shrinks the value by a factor of 40, it can be calculated that the rms value of DC component of the output voltage u_{Co} is around 7.8V*40 = 312V and the rms value of DC component of u_{C2}

is around 9.0V*40 = 360V. And similarly, the rms value of ripple of the output voltage u_{Co} is 372.08m*40 = 14.8832V when $\beta_1 = 1.05$, it is 415.60m*40 = 16.624V when $\beta_1 = 1.00$, it is 563.65mV*40 = 22.546V when $\beta_1 = 0.95$, and it is 633.06mV*40 = 25.3224V when $\beta_1 = 0.90$. It can be seen that the experimental results and the simulation results in *Simulation scenario II* are generally consistent. Therefore, it verifies that the ripple of the output voltage increases as the capacitor order β_1 decreases.

Fig. 15 shows the influence of the qZS network inductor order α_2 on the experimental waveforms of inductor current and capacitor voltage. In this experiment, i_{L2} stabilizes at about 8A, u_{C2} stabilizes at about 360V and u_{Co} stabilizes at about 320V. As shown in Fig. 15, the rms value of ripple of i_{L2} is 2.2862A when $\alpha_2 = 1.0$, Δi_{L2} is 4.4583A when $\alpha_2 = 0.95$ and Δi_{L2} is 5.5260A when $\alpha_2 = 0.9$. The rms value of ripple of u_{C2} is 447.21m*40 = 17.8884V when $\alpha_2 = 1.0$ and Δu_{C2} is 487.89m*40 = 19.5156V when $\alpha_2 = 0.95$. The rms value of ripple of u_{Co} is 310.83m*40 = 12.4332V when $\alpha_2 = 1.0$, Δu_{Co} is 558.32m*40 = 22.3328V when $\alpha_2 = 0.95$ and Δu_{Co} is 738.99m*40 = 29.5596V when $\alpha_2 = 0.9$. Therefore, one can find that the trend exhibited by above experimental results are almost essentially the same as the trend exhibited by simulation results in *Simulation scenario III*. Hence, it can be concluded that the ripples of i_{L1}, i_{L2}, u_{C1}, u_{C2} and u_{Co} increase with α_2 decreasing, which is same as the theoretical analysis and simulation results.

Fig. 16 shows the influence of the qZS network capacitor order β_2 on the experimental waveforms of inductor current and capacitor voltage. In this experiment, i_{L2} stabilizes at about 8A, u_{C2} stabilizes at about 360V and u_{Co} stabilizes at about 320V. Fig. 16 shows that the rms value of ripple of i_{L2} is 2.2862A when $\beta_2 = 1.0$, Δi_{L2} is 3.1535A when $\beta_2 = 0.95$ and Δi_{L2} is 4.3844A when $\beta_2 = 0.9$. The rms value of ripple of u_{C2} is 447.21m*40= 17.8884V when $\beta_2 = 1.0$, Δu_{C2} is 565.17m*40 = 22.6068V when $\beta_2 = 0.95$ and Δu_{C2} is 846.29m*40 = 33.8516V when $\beta_2 = 0.9$. The rms value of ripple of u_{Co} is 310.83m*40 = 12.4332V when $\beta_2 = 1.0$, Δu_{Co} is 429.30m*40 = 17.172V when $\beta_2 = 0.95$ and Δu_{Co} is 542.09m*40 = 21.6836V when $\beta_2 = 0.9$. Therefore, one can find that the trend exhibited by above experimental values are essentially the same as the trend exhibited by simulation results in *Simulation scenario III*. And the ripples of i_{L1}, i_{L2}, u_{C1}, u_{C2} and u_{Co} increase with the capacitor order β_2 decreasing, which are also the same as the theoretical analysis and simulation results. With the help of the RT-LAB platform, the experimental results verify the correctness of the above analysis and results.

IX. CONCLUSION

In this paper, the model of single-phase FO-qZSR is proposed. We analyze the modeling and characteristics of single-phase qZSR in fractional-order field. The conventional integer-order model is included in the range of fractional-order model, and it is a special case of FO-qZSR. The working princicle, control strategy, modulation scheme and operating characteristics of FO-qZSR are analyzed in detail. Additionally, based on the circuit model of FOI/FOC using Oustaloup's approximation method, and the mathematical model of FO-PI$^{\lambda}$ D$^{\mu}$ controller, we have simulated the circuit model of FO-qZSR to verify the above theoretical analysis. And the experimental verifications are performed with the help of semi-physical hardware-in-loop RT-LAB platform. The experiment results are consistent with the theoretical analysis and simulation results. The research of grid side input current, inductor current, capacitor voltage and output voltage show that the order of FOI/FOC will dramatically affect the operating characteristics of FO-qZSR. The grid side inductor order α_1 and output capacitor order β_1 have an impact on the grid side current and output voltage. The qZS network inductor order α_2 and capacitor order β_2 have an influence on inductor current, capacitor voltage, grid side current and the output voltage. Compared with the conventional single-phase IO-qZSR, the single-phase PWM FO-qZSR has more flexible output voltage, more diversified and elastic operating characteristics, and may obtain better dynamic and static properties by choosing the appropriate orders of fractional-order inductor and capacitor.

REFERENCES

[1] Y. Chen, I. Petras, and D. Xue, "Fractional-order control: A tutorial," in *Proc. Amer. Control Conf. (ACC)*, St. Louis, MO, USA, Jun. 2009, pp. 1397–1411.

[2] M. Axtell and M. E. Bise, "Fractional calculus application in control systems," in *Proc. IEEE Conf. Aerosp. Electron.*, May 1990, pp. 563–566.

[3] J. C. Trigeassou, T. Poinot, J. Lin, A. Oustaloup, and F. Levron, "Modeling and identification of a non integer order system," in *Proc. Eur. Control Conf. (ECC)*, Aug. 1999, pp. 2453–2458.

[4] I. Podlubny, "Fractional-order systems and PI$^{\lambda}$Dμ controllers," *IEEE Trans. Autom. Control*, vol. 44, no. 1, pp. 208–214. Jan. 1999.

[5] X. Chen, L. Xi, Y. Zhang, H. Ma, Y. Huang, and Y. Chen, "Fractional techniques to characterize non-solid aluminum electrolytic capacitors for power electronic applications," *Nonlinear Dyn.*, vol. 98, no. 4, pp. 3125–3141, Dec. 2019.

[6] T. J. Freeborn, B. Maundy, and A. S. Elwakil, "Measurement of supercapacitor fractional-order model parameters from voltage-excited step response," *IEEE J. Emerg. Sel. Topics Circuits Syst.*, vol. 3, no. 3, pp. 367–376, Sep. 2013.

[7] S. Westerlund and L. Ekstam, "Capacitor theory," *IEEE Trans. Dielectr. Electr. Insul.*, vol. 1, no. 5, pp. 826–839, Oct. 1994.

[8] A. G. Radwan, A. Shamim, and K. N. Salama, "Theory of fractional order elements based impedance matching networks," *IEEE Microw. Wireless Compon. Lett.*, vol. 21, no. 3, pp. 120–122, Mar. 2011.

[9] A. G. Radwan and K. N. Salama, "Passive and active elements using fractional $L_{\beta}C_{\alpha}$ circuit," *IEEE Trans. Circuits Syst. I, Reg. Papers*, vol. 58, no. 10, pp. 2388–2397. Oct. 2011.

[10] J. Valsa, "Fractional—Order electrical components, networks and systems," in *Proc. 22nd Int. Conf. Radioelektronika*, Apr. 2012, pp. 1–9.

[11] D. Mondal and K. Biswas, "Packaging of single-component fractional order element," *IEEE Trans. Device Mater. Rel.*, vol. 13, no. 1, pp. 73–80, Mar. 2013.

[12] A. K. Jonscher, "Dielectric relaxation in solids," *J. Phys. D, Appl. Phys.*, vol. 32, pp. R57–R70, 1999.

[13] G. W. Bohannan, "Interpretation of complex permittivity in pure and mixed crystals," *AIP Conf. Proc.*, vol. 535, pp. 250–258, Dec. 2000.

[14] I. S. Jesus and J. A. T. Machado, "Development of fractional order capacitors based on electrolyte processes," *Nonlinear Dyn.*, vol. 56, nos. 1–2, pp. 45–55, Apr. 2009.

[15] S. Westerlund, "Dead matter has memory!" *Phys. Scripta*, vol. 43, no. 2, pp. 174–179, Feb. 1991.

[16] J. A. Tenreiro Machado and A. M. S. F. Galhano, "Fractional order inductive phenomena based on the skin effect," *Nonlinear Dyn.*, vol. 68, nos. 1–2, pp. 107–115, Apr. 2012.
[17] A. Oustaloup, F. Levron, B. Mathieu, and F. M. Nanot, "Frequency-band complex noninteger differentiator: Characterization and synthesis," *IEEE Trans. Circuits Syst. I, Fundam. Theory Appl.*, vol. 47, no. 1, pp. 25–39, Jan. 2000.
[18] X. Chen, Y. Chen, B. Zhang, and D. Qiu, "A modeling and analysis method for fractional-order DC–DC converters," *IEEE Trans. Power Electron.*, vol. 32, no. 9, pp. 7034–7044, Sep. 2017.
[19] A. G. Radwan, A. A. Emira, A. M. Abdelaty, and A. T. Azar, "Modeling and analysis of fractional order DC–DC converter," *ISA Trans.*, vol. 82, pp. 184–199, Nov. 2018.
[20] Z. Wei, B. Zhang, and Y. Jiang, "Analysis and modeling of fractional-order buck converter based on Riemann–Liouville derivative," *IEEE Access*, vol. 7, pp. 162768–162777, 2019.
[21] F.-Q. Wang and X.-K. Ma, "Transfer function modeling and analysis of the open-loop buck converter using the fractional calculus," *Chin. Phys. B*, vol. 22, no. 3, Mar. 2013, Art. no. 030506.
[22] B. Babes, S. Mekhilef, A. Boutaghane, and L. Rahmani, "Fuzzy approximation-based fractional-order nonsingular terminal sliding mode controller for DC–DC buck converters," *IEEE Trans. Power Electron.*, vol. 37, no. 3, pp. 2749–2760, Mar. 2022.
[23] T. Cheng and L. Zhi-Shan, "Modeling and simulation analysis of fractional-order boost converter in pseudo-continuous conduction mode," *Acta Phys. Sinica*, vol. 63, no. 7, 2014, Art. no. 070502.
[24] Y. Chen, X. Chen, J. Hu, B. Zhang, and D. Qiu, "A symbolic analysis method for fractional-order boost converter in discontinuous conduction mode," in *Proc. IECON*, Beijing, China, Sep. 2017, pp. 8738–8743.
[25] F. Wang and X. Ma, "Fractional order buck–boost converter in CCM: Modelling, analysis and simulations," *Int. J. Electron.*, vol. 101, no. 12, pp. 1671–1682, Dec. 2014.
[26] C. Wu, G. Si, Y. Zhang, and N. Yang, "The fractional-order state-space averaging modeling of the buck–boost DC/DC converter in discontinuous conduction mode and the performance analysis," *Nonlinear Dyn.*, vol. 79, no. 1, pp. 689–703, Jan. 2015.
[27] P. Zhu, Y. Wei, Z. Zheng, X. Wang, and F. Ma, "Fractional modelling and simulation for single-phase PWM rectifier," *J. Eng.*, vol. 2019, no. 16, pp. 1675–1678, Mar. 2019.
[28] J. Xu, X. Li, X. Meng, J. Qin, and H. Liu, "Modeling and analysis of a single-phase fractional-order voltage source pulse width modulation rectifier," *J. Power Sources*, vol. 479, Dec. 2020, Art. no. 228821.
[29] T. Shi, Y. He, T. Wang, J. Tong, B. Li, and F. Deng, "An improved open-switch fault diagnosis technique of a PWM voltage source rectifier based on current distortion," *IEEE Trans. Power Electron.*, vol. 34, no. 12, pp. 12212–12225, Dec. 2019.
[30] S. Xie, Y. Sun, J. Lin, M. Su, X. Li, and X. Zhang, "Resistance-emulating control strategy for three-phase voltage source rectifiers under unbalanced grids," *IEEE Trans. Ind. Electron.*, vol. 69, no. 2, pp. 1103–1113, Feb. 2022.
[31] X. Ding, K. Li, Y. Hao, H. Li, and C. Zhang, "Family of the coupled-inductor multiplier voltage rectifier quasi-Z-source inverters," *IEEE Trans. Ind. Electron.*, vol. 68, no. 6, pp. 4903–4915, Jun. 2021.
[32] X. Ding, F. Wang, M. Zhou, Y. Cao, and Z. Wei, "Soft switching high voltage gain quasi-Z-source DC–DC converter with switched-capacitor technique," *IEEE Trans. Ind. Electron.*, vol. 69, no. 11, pp. 11231–11241, Nov. 2022.
[33] A. Nafari and R. Beiranvand, "An extendable interleaved quasi Z-source high step-up DC–DC converter," *IEEE Trans. Power Electron.*, vol. 38, no. 4, pp. 5065–5076, Apr. 2023.
[34] T. Na, Q. Zhang, J. Tang, and J. Wang, "Active power filter for single-phase quasi-Z-source integrated on-board charger," *CPSS Trans. Power Electron. Appl.*, vol. 3, no. 3, pp. 197–201, Sep. 2018.
[35] T. Na, Q. Zhang, G. Xu, Y. Yan, and X. Chen, "A modified SVM method for three-phase quasi-Z-source rectifier with fully soft switching operation and low conduction losses," *IEEE Trans. Ind. Electron.*, vol. 70, no. 8, pp. 7547–7556, Aug. 2023.
[36] Z. Chen, X. Zhu, and J. Hou, "Modeling and analysis of single-phase fractional-order quasi-Z-source rectifier," in *Proc. IEEE 2nd Int. Power Electron. Appl. Symp. (PEAS)*, Guangzhou, China, Nov. 2023, pp. 86–91, doi: 10.1109/peas58692.2023.10395791.
[37] K. C. and U. M. G., "Design of gray wolf optimizer algorithm-based fractional order PI controller for power factor correction in SMPS applications," *IEEE Trans. Power Electron.*, vol. 35, no. 2, pp. 2100–2118, Feb. 2020.
[38] K. Erenturk, "Fractional-order $PI^{\lambda}D^{\mu}$ and active disturbance rejection control of nonlinear two-mass drive system," *IEEE Trans. Ind. Electron.*, vol. 60, no. 9, pp. 3806–3813, Sep. 2013.
[39] P. Chen and Y. Luo, "Analytical fractional-order PID controller design with Bode's ideal cutoff filter for PMSM speed servo system," *IEEE Trans. Ind. Electron.*, vol. 70, no. 2, pp. 1783–1793, Feb. 2023.

XIAOQUAN ZHU (Senior Member, IEEE) was born in Anhui, China, in 1990. He received the B.S. degree from the School of Information and Control Engineering, China University of Mining and Technology, Xuzhou, China, in 2014, and the Ph.D. degree in power electronics from the School of Electric Power Engineering, South China University of Technology, Guangzhou, China, in 2019.

He is currently a Lecturer with the College of Automation Engineering, Nanjing University of Aeronautics and Astronautics, Nanjing, China. His current research interests include renewable energy power generation systems and fractional-order modeling and control of power converters.

ZIWEN CHEN was born in Jinan, China, in 2000. She received the B.S. degree from the College of Automation and Electronic Engineering, Qingdao University of Science and Technology, Qingdao, China, in 2022. She is currently pursuing the M.S. degree with Nanjing University of Aeronautics and Astronautics, Nanjing, China.

Her current research interests include fractional-order modeling and control of power converters.

BO ZHANG (Fellow, IEEE) was born in Shanghai, China, in 1962. He received the B.S. degree in electrical engineering from Zhejiang University, Hangzhou, China, in 1982, the M.S. degree in power electronics from Southwest Jiaotong University, Chengdu, China, in 1988, and the Ph.D. degree in power electronics from Nanjing University of Aeronautics and Astronautics, Nanjing, China, in 1994.

He is currently a Professor with the School of Electric Power, South China University of Technology, Guangzhou, China. He has authored or co-authored six books in IEEE-Wiley and Springer, more than 450 technical articles, and holds 100 patents. His current research interests include nonlinear analysis, modeling and control of power electronic converters, and wireless power transfer applications.